

**CRUSTAL STRUCTURE OF THE TIBETAN PLATEAU AND ITS  
SURROUNDINGS FROM RECEIVER FUNCTION STUDIES**

Yuming Zhou, B.S

An Abstract Presented to the Graduate Faculty of  
Saint Louis University in Partial Fulfillment  
of the Requirements for the Degree of  
Doctor of Philosophy

2013

## Abstract

The Tibetan Plateau is the highest and largest plateau in the world, generated by the collision of India and Eurasia. Details of this continent-continent collision and the uplift mechanism of the plateau are still hotly debated. In this study, I collected a large amount of seismic waveform data recorded by more than 300 stations in Tibet and its northern neighbor Tien Shan. I processed the data using teleseismic receiver function techniques to image crustal structures beneath the Himalayas, the southern Tibet plateau, and Tien Shan.

The results of receiver function studies show gentle northward dipping Moho beneath the Himalayas and increase of the dip of subduction near the Yarlung-Zangbo Suture, the boundary between the India plate and Tibet. This suggests that the Indian continental lithosphere is subducting underneath Tibet and the front of the Indian slab in the uppermost mantle is near the Yarlung-Zangbo Suture. I also found that the crustal  $V_p/V_s$  ratios (Ratios between seismic  $P$  wave velocity and  $S$  wave velocity) are consistently low in the Himalayas and are mixed with high and low  $V_p/V_s$  ratios in the Tibetan Plateau. This suggests that only limited and localized partial melting exists in the mid and lower crust in the southern and central Tibetan Plateau.

I determined crustal structures in and around the the Yadong-Gulu rift, the largest north-south-trending rift in southern Tibet, using receiver function techniques and joint-inversion technique with surface wave dispersion data. The results show a narrow zone beneath the rift where the crustal structure is different from outside the rift. This indicates that the east-west extension deformation of the Tibetan Plateau is localized in several narrow vertical zones through the entire crust.

The Tien Shan in central Asia is the largest and most active intra-continental orogen in the world. This mountain range is located nearly 2000 km north of the

Indian and Asian collision front. I also used a receiver function techniques to study this region. The results show no dipping Moho beneath its southern edge with the Tarim basin. However, a southward dipping interface can be seen beneath its northern edge with the Kazakh Shield. The Moho becomes shallower beneath the Naryn Basin in the interior of Tien Shan. The results suggest that the uplift of Tien Shan is due to a combination of horizontal shortening from the India-Tibet collision and mantle upwelling from below.



**CRUSTAL STRUCTURE OF THE TIBETAN PLATEAU AND ITS  
SURROUNDINGS FROM RECEIVER FUNCTION STUDIES**

Yuming Zhou, B.S

A Dissertation Presented to the Graduate Faculty of  
Saint Louis University in Partial Fulfillment  
of the Requirements for the Degree of  
Doctor of Philosophy

2013

UMI Number: 3611062

All rights reserved

INFORMATION TO ALL USERS

The quality of this reproduction is dependent upon the quality of the copy submitted.

In the unlikely event that the author did not send a complete manuscript and there are missing pages, these will be noted. Also, if material had to be removed, a note will indicate the deletion.



UMI 3611062

Published by ProQuest LLC (2014). Copyright in the Dissertation held by the Author.

Microform Edition © ProQuest LLC.

All rights reserved. This work is protected against unauthorized copying under Title 17, United States Code



ProQuest LLC.  
789 East Eisenhower Parkway  
P.O. Box 1346  
Ann Arbor, MI 48106 - 1346

© Copyright by  
Yuming Zhou  
ALL RIGHTS RESERVED

2013

COMMITTEE IN CHARGE OF CANDIDACY:

Professor Lupei Zhu

Chairperson and Advisor

Associate Professor John Encarnacion

Assistant Professor Linda M. Warren

## **Dedication**

This dissertation is dedicated to my mother.

## Acknowledgments

During my five and half years of graduate study at the Department of Earth and Atmospheric Sciences, what typically sticks in my memory is the oxygen-rich atmosphere favorable to the growth of both knowledge and friendship.

I have had much generous help and guidance from faculty members and staff as well as my classmates and officemates. I am deeply grateful to my adviser, Dr. Lupei Zhu, for his support throughout, his encouragement, his valuable suggestions and smart ideas, and for helping me improve the way I do research. He contributed greatly to my dissertation development and influenced my sense of what seismology is all about. Under his guidance, I learned how to enjoy each wiggle of seismograms. I also enjoyed inspecting P wave arrival time and receiver functions. I want to acknowledge the committee members, Drs. Linda M. Warren and John Encarnacion for their comments, reviews and fruitful lectures.

I want to acknowledge Drs. Robert B. Herrmann, David L. Kirschner, and David J. Crossley for their contributions to this effort.

I am thankful to Eric J. Haug and Bob Wurth for their support which has solved many of my computer-related problems. I wish to thank Edwards Loretta and Laurie Hausmann for providing all the needed assistance. And I shall also mention interesting conversations I had with Melanie Whittington.

I am grateful to Hongfeng Yang, Aihua Yan, Ming Zhu, Yagang Wang, Guangzhi Huang, Xiaoyu Guo, Xiao Xu, Lei Qiao, Lei Yang, Lulin Xue who helped me to settle down at Saint Louis University in the first year. I thank Hongfeng Yang for being a big brother, senior fellow mentor and good friend of mine, and his wife Aihua Yang for her help. I also thank Louisa Barama, Shan Bi, Ying Chang, Xiaoxue Ding, Rose Gabbert, Shaoqian Hu, Timothy Keenan, Patrick Luetkemeyer, Fang Ren, Ying Song, Oner Sufri, Yan Xu, Ke Deng, Wensu Liu, Junyong Chang,

Wanrou Chen, Yang Li, Xiaolong Lv, Ju Zhang, Qian Nie, Lingpeng Zheng, and other graduate students for their friendship.

I thank Dr. Xiaodong Song at UIUC for his kindly offering the surface wave dispersion data of the Tibetan Plateau and numerous help, and Dr. Eric Sandvol at University of Missouri-Columbia for involving me in fieldwork in central China.

I wish to thank Joy Zhu, who has helped me in many difficult moments since I came to Saint Louis. With her kindness friendship, there is always warmness in my heart.

I must give my special gratitude to Drs. Qijia Tang, Xiaobo Tian, Yun Chen, Rong Huang, Xingchen Wang, and Yan Wu, who as visiting scholars to the department played a very important role when I was feeling down and supported me all the time. With their understanding, concerning and generous assistance, I can always feel light on my path and touching in my heart.

I also thank other visiting scholars Zijiang Yang, Xian Lan, Cheng Wang, Fang Xia, Lu Wen, Yonggang Ma, Changjiang Yin, Li Gu, Xinglai Shao, Jinlin Wang, and Ka A for many suggestions, encouragement, meals, and friendship.

Finally, no accounting of my indebtedness would be appropriated without thanking my family for their support throughout my education, especially my mother and father who instilled in me an appreciation for the power of learning and convinced me I could do it all the way through.

## Table of Contents

List of Figures . . . . .	viii
Chapter 1: Introduction . . . . .	1
Chapter 2: Methods . . . . .	5
2.1 Receiver functions . . . . .	5
2.1.1 Definition of receiver functions . . . . .	5
2.1.2 Time-domain iterative deconvolution . . . . .	7
2.2 H- $\kappa$ stacking . . . . .	8
2.3 CCP stacking . . . . .	12
Chapter 3: Crustal Structural Variation of the Southern and Central Tibetan Plateau from Teleseismic Receiver Function Studies . . . . .	14
3.1 Introduction . . . . .	14
3.2 Data . . . . .	18
3.3 Results . . . . .	23
3.3.1 H- $\kappa$ stacking results . . . . .	23
3.3.2 CCP stacking results . . . . .	24
3.4 Discussion . . . . .	28
3.4.1 Collision model . . . . .	28
3.4.2 Crustal structure beneath the BNS . . . . .	31
3.4.3 Partial melting in the southern and central Tibet . . . . .	32
3.5 Conclusions . . . . .	34
Chapter 4: Evidence of Coupled Deformation of Tibetan Crust Underneath the Northern Yadong-Gulu Rift . . . . .	35
4.1 Introduction . . . . .	35
4.2 Data and Methods . . . . .	39
4.2.1 Data processing and receiver functions . . . . .	39
4.2.2 H- $\kappa$ determination . . . . .	39
4.2.3 CCP imaging . . . . .	40
4.2.4 1-D velocity model from joint-inversion . . . . .	41
4.3 Discussion . . . . .	46
4.3.1 Structure inside the northern Yadong-Gulu Rift . . . . .	46
4.3.2 Structure outside the northern Yadong-Gulu Rift . . . . .	47
4.4 Conclusion . . . . .	48
Chapter 5: Crustal Structure of the Central Tien Shan Orogenic Belts from Receiver Function Studies . . . . .	49
5.1 Introduction . . . . .	49
5.2 Data . . . . .	53
5.3 Results from Receiver functions studies . . . . .	56
5.4 Discussion . . . . .	61
5.5 Conclusion . . . . .	64

References . . . . .	65
Vito Auctoris . . . . .	73

## List of Figures

Figure 1.1: This figure shows Tibetan Plateau and surrounding area, such as the Tarim Basin, Tian Shan, India, Qaidam Basin and Sichuan Basin. . . . .	1
Figure 2.1: The left figure shows the ray path, reflection and conversion of a teleseismic P wave among the crust. The right figure shows the receiver function computed for the simple structure. The relative amplitudes and arrival times depend on the layer velocities and thicknesses. (The left figure is from <a href="http://www.bssaonline.org/content/96/1/328/F1.large.jpg">http://www.bssaonline.org/content/96/1/328/F1.large.jpg</a> ; The right figure is from <a href="http://eqseis.geosc.psu.edu/cammon/HTML/RftnDocs/rftn01.htm">http://eqseis.geosc.psu.edu/cammon/HTML/RftnDocs/rftn01.htm</a> ) . . . . .	7
Figure 2.2: Radial receiver function as a function of ray parameter $p$ for the Standard Southern California Velocity Model. the Moho converted phase $Ps$ and the multiples $PpPs$ , $PpSs$ and $PsPs$ are labeled. (from <i>Zhu and Kanamori [2000, P.2971]</i> ) . . . . .	10
Figure 2.3: (a) The $s(H,\kappa)$ from stacking the receiver functions in Fig. 2.2. It reaches the maximum (solid area) when the correct crustal thickness and $Vp/Vs$ ratio are used in the stacking. (b) $H-\kappa$ relations for different Moho converted phases in Fig. 2.2. Each curve represents the contribution from this converted phase to the stacking. (from <i>Zhu and Kanamori [2000, P.2972]</i> ) . . . . .	11
Figure 2.4: Amplitude and variance (given by the contours) of CCP stacking for a profile across the San Andreas Fault in southern California. No vertical exaggeration except that the surface topography is amplified by a factor of 2. (from <i>Zhu [2000, P.186]</i> ) . . . . .	13
Figure 3.1: Map of the Tibetan Plateau and surrounding areas. MBT: the Main Boundary Thrust; YZS: the Yarlung-Zangbo suture; BNS: the Bangong-Nujiang suture; JRS: the Jinsha River suture. . . . .	15
Figure 3.2: The upper cartoon shows the India lower crust and mantle lithosphere subducting beneath YZS; The lower cartoon shows the Indian plate shortening horizontally and thickening vertically. The red thick lines represent the Moho. MHT: Main Himalaya Thrust. MCT: Main Central Thrust. LAB: Lithosphere Asthenosphere Boundary. . . . .	16

Figure 3.3: Locations of 322 stations from the four projects used in this study (Blue triangles show the HiClimb array, magenta triangles the INDEPTH I & II array, red triangles the Himalayan Nepal Tibet Experiment array and black triangles the Namche Barwa Tibet array). BNS stands for Bangong-Nujiang Suture. YZS stands for Yarlung-Zangbo Suture. The black lines are the CCP imaging profiles of each array. . . . .	20
Figure 3.4: Locations of broadband stations of the four arrays are shown as black triangles. The blue circles are the selected events recorded by the arrays. . . . .	21
Figure 3.5: <i>P</i> -wave records from an earthquake on October 12, 2002. The vertical black line aligns the first <i>P</i> -wave arrival times at all stations from the Hi-Climb array. The red trace is a bad record identified automatically by the multi-station waveform cross-correlation processing. . . . .	22
Figure 3.6: The V <sub>p</sub> /V <sub>s</sub> ratios are shown in colored circles. Blue means higher than the average value. Red means lower than the average V <sub>p</sub> /V <sub>s</sub> ratio. . . . .	24
Figure 3.7: CCP stacking images along profiles shown in Black lines in Fig. 3.3. From the top to bottom, the images are from the Hi-Climb array, INDEPTH II and III array, Himalayan Nepal Tibet Experiment array, and Namche Barwa Tibet array, respectively. Amplitude shows the vertical velocity change. Positive value means velocity increase downward. Negative value means the opposite. All these images are aligned with the surface trace of YZS, which is marked 0 km on the horizontal axis. . . . .	26
Figure 3.8: CCP image along an east-west profile, centered at 93°E, 30°N. . . . .	28
Figure 3.9: Illustration of the oblique subduction of the Indian mantle lithosphere. The black line is the India-Asia plate boundary at the Moho level. The two blue lines are the surface boundary of YZS and BNS. . . . .	30
Figure 3.10: The Moho images of Indian mantle lithosphere from four arrays' receiver function results. Each color represents one array. These images are centered at YZS and show the Moho variation to a distance of 200 km north and south of the YZS. . . . .	31
Figure 4.1: Map of the Tibetan Plateau and India. The northern part of the Yadong-Gulu rift beyond YZS is the study area shown within a black square. MBT: the Main Boundary Thrust; YZS: the Yarlung-Zangbo suture; BNS: the Bangong-Nujiang suture; JRS: the Jinsha River suture. . . . .	36

Figure 4.2: Summary of the effects of lower crustal decoupling/coupling on the symmetry of extension. UC upper crust, LC lower crust, UML upper mantle lithosphere, LML lower mantle lithosphere [Reston and Perez-Gussinye, 2007]. . . . .	37
Figure 4.3: All stations are represented by circles. Receiver functions from stations represented by the red circles are utilized to do H- $\kappa$ stacking and CCP stacking. The black line orientated northwest-southeast is the location of the CCP profile. . . . .	40
Figure 4.4: Radial receiver function as a functions of ray parameter $p$ for the 1-D Tibetan Plateau Velocity Model [Zhu, 2003]. the Moho converted phase $Ps$ and the multiples $PpPs$ , $PpSs$ and $PsPs$ are labeled. . . . .	43
Figure 4.5: The $s(H,\kappa)$ from stacking the receiver functions in Fig. 2.2. It reaches the maximum (solid area) when the correct crustal thickness and $Vp/Vs$ ratio are used in the stacking. . . . .	44
Figure 4.6: The upper figure is the CCP image from profile AB in Fig. 4.3. The red color and blue color represent top to bottom velocity increase or decrease respectively. The gray shape means no data coverage. . . . .	44
Figure 4.7: Relocations of 64 events using the array method. . . . .	45
Figure 5.1: Map of the research area. The blue triangles are the stations from NANGA KNET, GSN, GEOSCOPE and GHENGIS networks. The KAI and NRN stations are in the Naryn Basin and are utilized to perform the surface-wave and receiver function joint-inversion. Two profiles AB and CD oriented from northwest to southeast are used to image the crustal structure. . . . .	50
Figure 5.2: The top figure is a sketch of underthrusting model. The bottom figure is a sketch of horizontal shortening model. . . . .	51
Figure 5.3: Locations of the 53 broadband stations in the research area are shown as black triangles. The blue circles are the selected events recorded by these stations. . . . .	54
Figure 5.4: Teleseismic $P$ wave receiver functions plotted in the order of back-azimuth. R and T represent radial and transverse components, respectively. . . . .	55
Figure 5.5: The crustal structure imaged by CCP stacking method along the western profile in Fig. 5.1. The black crosses show the crustal thickness from the H- $\kappa$ stacking method. . . . .	58
Figure 5.6: The crustal structure imaged by CCP stacking method along the eastern profile in Fig. 5.1. . . . .	59

Figure 5.7: The left panel is the joint-inversion result of station KAI. The right panel is the result of station NRN. For each panel, the left box is 1-D S-wave velocity profile (in black color). The right top figure is surface wave dispersions. Black dots are real data, red line is the joint-inversion result. Receiver functions are shown at the bottom (Red traces are synthetic receiver functions). . . . .

60

Figure 5.8: The top figure shows the initial configuration before the uplift of the Tien Shan. The Kazakh Shield is fixed and the Tarim basin is moving towards the Tien Shan. The middle figure shows an interpretation of CCP image of profile AB, the bottom shows an interpretation of CCP image of profile CD. . . . .

63

## Chapter 1: Introduction

The Tibetan Plateau is located in central Asia. It has the highest average elevation of 5023 m and the largest area of about 3500 by 1500 km<sup>2</sup> in the world, which accounts for 82% of the area over 4 km above sea level. The Tibetan Plateau is composed of continental fragments added successively to the southern Asian margin over the past 50 Ma. The fragments, from north to south, include the Songpan Ganzi Terrane, Qiangtang Terrane, and Lhasa Terrane. The surrounding areas of the Tibet include the Indian plate to the south, the Tarim Basin to the northwest and the Sichuan Basin to the southeast. The Indian plate is separated from the plateau by the Yarlung-Zangpo Suture (YZS). The Tarim Basin is located between the Tibetan Plateau and the Tien Shan Mountian range (Fig. 1.1).

The development of the Cenozoic Tibetan plateau began in the Eocene about

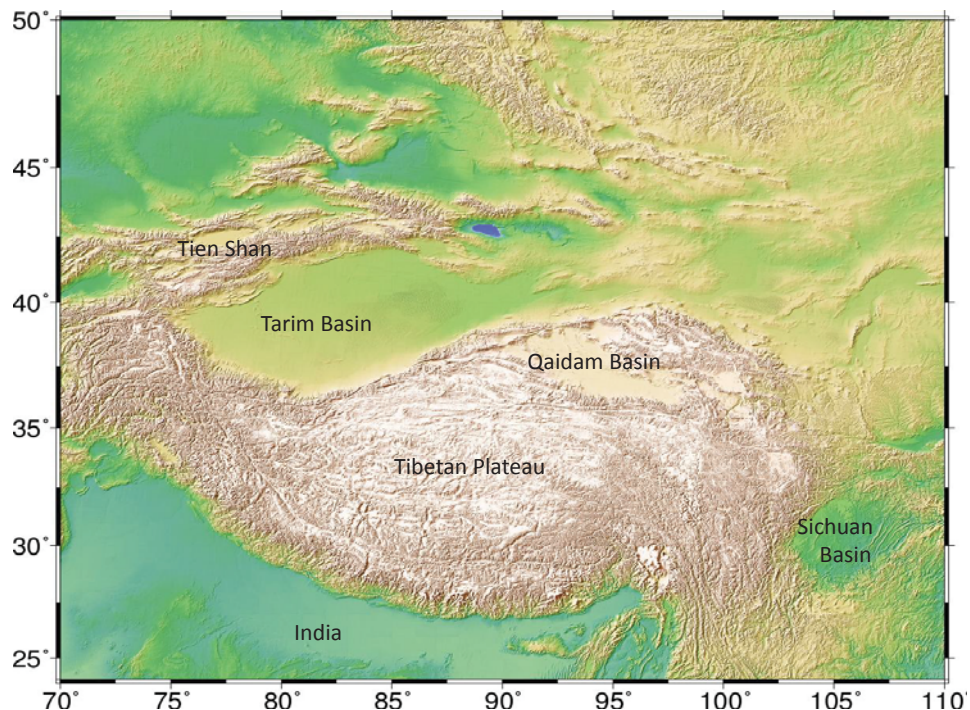


Figure 1.1: This figure shows Tibetan Plateau and surrounding area, such as the Tarim Basin, Tian Shan, India, Qaidam Basin and Sichuan Basin.

50–40 Ma with the onset of collision between the Indian and Asian Plates [*Patriat and Achache*, 1984]. The collision results in an anomalously thick continental crust of 70–90 km [*Mejia*, 2001]. Uplift of the plateau started in the middle Eocene (45 Ma) [*Patriat and Achache*, 1984] and began to accelerate at about 8 Ma [*Molnar et al.*, 1993]. The Tibetan lithosphere also experienced east-west extension, resulting in a rift system distributed across the plateau [*Molnar and Tapponnier*, 1978]. The Tien Shan orogeny resumed at about 20 Ma, which is presumably attributed to the Indian-Asian collision [*Sobel and Dumitru*, 1997; *Yin et al.*, 1998].

How such a high plateau was formed has been a focus of international geological and geophysical research since the 1970s. So far, several end-member models have been proposed for the India-Asia collision and uplift of the Tibetan Plateau. Most of the previous models invoke crustal interactions to explain the uplifting of the Tibetan Plateau. This study seeks to understand the role of Indian mantle lithosphere processes in the framework of plate tectonics in order to further improve collision models. The plate tectonics theory has been successfully applied to oceanic plates, shows that the deformation zones are narrowly restricted to plate boundaries, assuming the oceanic lithosphere is relatively strong. In contrast, continental lithosphere often has broad zones of deformation that are heterogeneously distributed. The Indian-Asian collision zone provides an excellent natural laboratory to investigate how large plateaus form as a result of continent-continent collision.

The Tien Shan, north of the Tibetan Plateau is the largest and most active intercontinental orogen in last 20 Ma. The ancestral Tien Shan formed in the Paleozoic and subsequent erosion resulted in a peneplain by the Mesozoic [*Dobretsov and Zagruzina*, 1977; *Avouac and Tapponnier*, 1993]. The Indian-Asian Collision likely reactivated the Tien Shan's orogenic activity at about 20 Ma [*Sobel and Dumitru*, 1997; *Yin et al.*, 1998]. The Tien Shan and the Tibetan Plateau are similar in that they both were formed by collisional processes, involving blocks of

continental lithosphere. Thus, the Tien Shan is also a prime candidate for studies about uplift and deformation during convergence between continental lithospheres.

Most of the large scale surface structures within the Tibetan Plateau, such as the Jinsha-River Suture (JRS), Bangong-Nujiang Suture(BNS), and the Yarlung-Zangpo Suture, are east-west oriented. This orientation is consistent with north-south directed collision. North-south trending normal faults and rift systems are also present on Tibet. To model the plate-like behavior of continental lithosphere, one assumes that the continental blocks are separated by localized deformation penetrating through the entire lithosphere [*Tapponnier et al.*, 1982; *Peltzer and Tapponnier*, 1988; *Avouac and Tapponnier*, 1993]. The second model in which the continental lithosphere deformed, is continuum lithosphere model. Thin viscous sheet are normally applied to simulate the continuous deformation of continental lithosphere, which generates wider zones of deformation in or near the plate boundary [*Bird and Piper*, 1980; *England and McKenzie*, 1982; *Vilotte et al.*, 1982; *England and Houseman*, 1986]. The present investigation focus on how these rift systems formed, and seeks to answer the question: Does continental lithosphere deform continuously or rigidly?

To study these problems, I used receiver function methods. I collected and processed *P*-wave waveform data of teleseismic events recorded by all available arrays deployed in the Tien Shan, Tarim Basin and Tibetan Plateau. Teleseismic *P*-wave receiver functions were calculated and processed using the Common-Conversion-Point (CCP) stacking, H- $\kappa$  stacking techniques and joint inversion with surface wave dispersion data to reveal Vp/Vs ratios (Ratios between seismic *P* wave velocity and *S* wave velocity) and seismic velocities beneath this area. I then analyzed and interpreted the results to explain how the continental lithosphere deformed during collision.

Chapter 2 discusses the advantages of the data processing methods and receiver

function techniques, used throughout the study. Chapter 3 summarizes the data sets obtained for the southern and central Tibet region, and investigates Moho (Boundary between crust and mantle) depth variation and  $V_p/V_s$  ratio of this region using receiver function techniques. Knowing where the Indian Moho is located can provide important constraints on Indian-Asian mantle lithosphere deformation during collision. In chapter 4, receiver function techniques are applied to several stations within and outside of the Yadong-Gulu rift. Joint inversion with the surface wave dispersion data are used to reveal the velocity structure beneath the rift and surrounding area. The comparision of the results inside and outside the rift can tell whether the anomalies are distributed regionally in the rift zone or through out the entire crust. Chapter 5 summarizes receiver function' results from 53 stations in the Tien Shan area. An attempt to explain the mechanism behind the revival of tectonic activity of Tien Shan orogen is then given, based on the seismic images of this region.

## Chapter 2: Methods

### 2.1 Receiver functions

#### 2.1.1 Definition of receiver functions

The receiver functions are sensitive to velocity contrasting interfaces in lithosphere, thus are widely used to image the crustal structure variation. To explain the definition of the receiver functions, we should begin with the original seismic data.  $P$ -wave seismic data contains three components: R (radial component), T (transverse component), and V (vertical component). The teleseismic  $P$ -wave waveform at a station,  $D(t)$ , can be theoretically represented by the following equations:

$$D_V(t) = I(t) * S(t) * E_V(t), \quad (2.1)$$

$$D_R(t) = I(t) * S(t) * E_R(t), \quad (2.2)$$

$$D_T(t) = I(t) * S(t) * E_T(t), \quad (2.3)$$

where subscripts V, R and T represent the vertical, radial, and transverse components respectively.  $I(t)$  is the impulse response of the recording instrument;  $S(t)$  is the seismic source time function;  $E(t)$  is the impulse response of the earth structure beneath the station; Asterisks represent the convolution operator. For teleseismic  $P$ -wave with a steep incident angle, the vertical component of the response consists of a large direct arrival and minor arrivals from reverberations and phase conversions in the crust. Therefore, *Langston* [1979] assumes that:

$$E_V(t) \approx \delta t, \quad (2.4)$$

where  $\delta t$  is the Dirac delta function. Then,

$$D_V(t) = I(t) * S(t). \quad (2.5)$$

Thus,  $D_V(t)$  is exactly the factor that can be removed from  $D_R(t)$  and  $D_T(t)$  to obtain the earth structure response  $E_R(t)$  and  $E_T(t)$ , respectively. To perform the deconvolution, horizontal components are divided by vertical components in the frequency domain after applying a Fourier transform. We can also exclude high-frequency noise by introducing a Gaussian function. This leaves the radial receiver function in the frequency domain as:

$$E_R(w) = \frac{D_R(w)D_{\bar{V}(w)}}{\varphi(w)}G(w), \quad (2.6)$$

where

$$\varphi(w) = \max(D_V(w)D_{\bar{V}(w)}, c \cdot \max[D_V(w)D_{\bar{V}(w)}]), \quad (2.7)$$

and

$$G(w) = e^{\frac{-w^2}{4\alpha^2}}. \quad (2.8)$$

In these expressions,  $c$  is the water level,  $\alpha$  controls the width of the Gaussian pulse and the bar over  $D_V$  indicates its complex conjugate. Then inverse Fourier transform converts  $E_R(w)$  back to the time domain, giving  $E_R(t)$  as the typical receiver function.

A  $P$ -to- $S$  conversion will occur when a seismic wave hits a velocity interface (i.e., a  $P$ -wave converts to an  $S$ -wave or an  $S$ -wave converts to a  $P$ -wave). In addition to the largest amplitude of direct  $P$  wave, a receiver function consists of a  $Ps$  phase and many multiples( $PpPs$ ,  $PsPs$  and  $PpSs$ ) (Fig. 2.1).  $Ps$  phase corresponds to a  $P$  to  $S$  conversion, that is then recorded by a receiver.  $PpPs$  phase is a  $P$  wave that is reflected at the free surface as a  $P$  wave, and then is reflected at the interface and

transfer to  $S$  wave and recorded by a receiver. Similarly,  $PpSs$  and  $PsPs$  have the same theoretical arrival time,  $PpSs$  goes through interface as  $P$  wave and reflected at free surface as  $S$  wave, but  $PsPs$  is opposite.

### 2.1.2 Time-domain iterative deconvolution

*Ligorria and Ammon* [1999] first introduced the time-domain iterative deconvolution method to compute receiver functions. Although this method is equally effective for estimating receiver functions and has a modest increase in computation costs, it has several important advantages. The time-domain iterative deconvolution can simply calculate receiver functions without considering the parameters, such as water-level, time-domain smoothing and damping parameters. First, the vertical component is cross-correlated with the radial component to estimate the lag of the first and largest peak in the receiver function. The peak amplitude is estimated by solving a simple equation listed in [*Kikuchi and Kanamori*, 1982]. Then the convolution of the current estimate of the receiver function with the vertical-component seismogram is subtracted from the

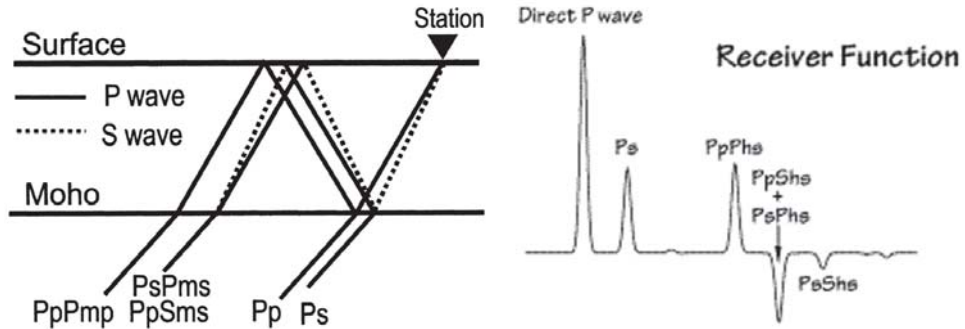


Figure 2.1: The left figure shows the ray path, reflection and conversion of a teleseismic  $P$  wave among the crust. The right figure shows the receiver function computed for the simple structure. The relative amplitudes and arrival times depend on the layer velocities and thicknesses. (The left figure is from <http://www.bssaonline.org/content/96/1/328/F1.large.jpg>; The right figure is from <http://eqseis.geosc.psu.edu/cammon/HTML/RftnDocs/rftn01.html>.)

radial-component seismogram, and the procedure is repeated to estimate other peaks (lags and amplitudes) until the misfit of between the convolution of vertical and receiver function, and the radial component becomes insignificant.

## 2.2 H- $\kappa$ stacking

The H- $\kappa$  stacking method developed by *Zhu and Kanamori* [2000] is used for finding the Moho depth and the Vp/Vs ratio beneath each station by stacking the teleseismic  $P$ -wave receiver functions, where  $H$  is the thickness of the crust (Moho depth), and  $\kappa$  is the Vp/Vs ratio. This method first tries different values of  $H$  and  $\kappa$ , depending on the crustal thickness and Vp/Vs ratio. Theoretical arrival times of  $Ps$ ,  $PpPs$ , and  $PsPs$  or  $PpSs$  phases are then calculated (Fig. 2.2). Based on the theoretical arrival time of each phase, all the receiver functions are stacked and the amplitude summation is computed as:

$$s(H, \kappa) = w_1 r(t_1) + w_2 r(t_2) - w_3 r(t_3), \quad (2.9)$$

where  $r(t)$  is the radial receiver function,  $t_1$ ,  $t_2$  and  $t_3$  are the theoretical  $Ps$ ,  $PpPs$  and  $PpSs + PsPs$  arrival times corresponding to assumed crustal thickness  $H$  and Vp/Vs ratio  $\kappa$ . The  $w_i$ 's are weighting factors, and

$$\sum w_i = 1. \quad (2.10)$$

The  $s(H, \kappa)$  reaches a maximum when all three phases are stacked coherently with the correct  $H$  and  $\kappa$  (Fig. 2.3).

The uncertainties can be estimated from the flatness of  $s(H, \kappa)$  at the maximum. Using the Taylor expansion of  $s(H, \kappa)$  at the maximum and neglecting the

higher-order terms, one can get the variances of  $H$  and  $\kappa$ :

$$\sigma_H^2 = 2\sigma_s / \frac{\partial^2 s}{\partial H^2}, \quad (2.11)$$

$$\sigma_\kappa^2 = 2\sigma_s / \frac{\partial^2 s}{\partial \kappa^2}, \quad (2.12)$$

where  $\sigma_s$  is the estimated variance of  $s(H, \kappa)$  from stacking.

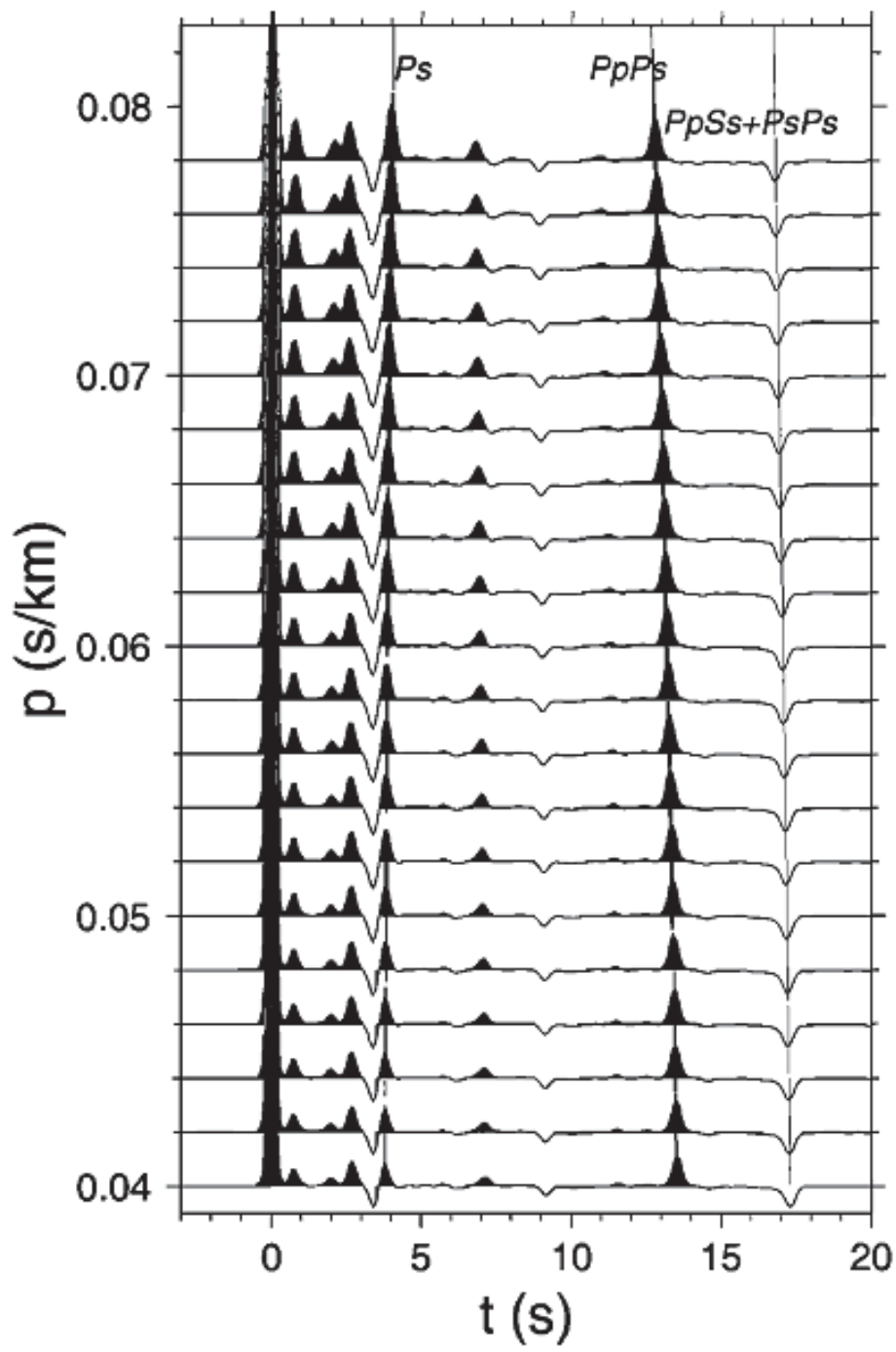


Figure 2.2: Radial receiver function as a function of ray parameter  $p$  for the Standard Southern California Velocity Model. the Moho converted phase  $Ps$  and the multiples  $PpPs$ ,  $PpSs$  and  $PsPs$  are labeled. (from *Zhu and Kanamori [2000, P.2971]*)

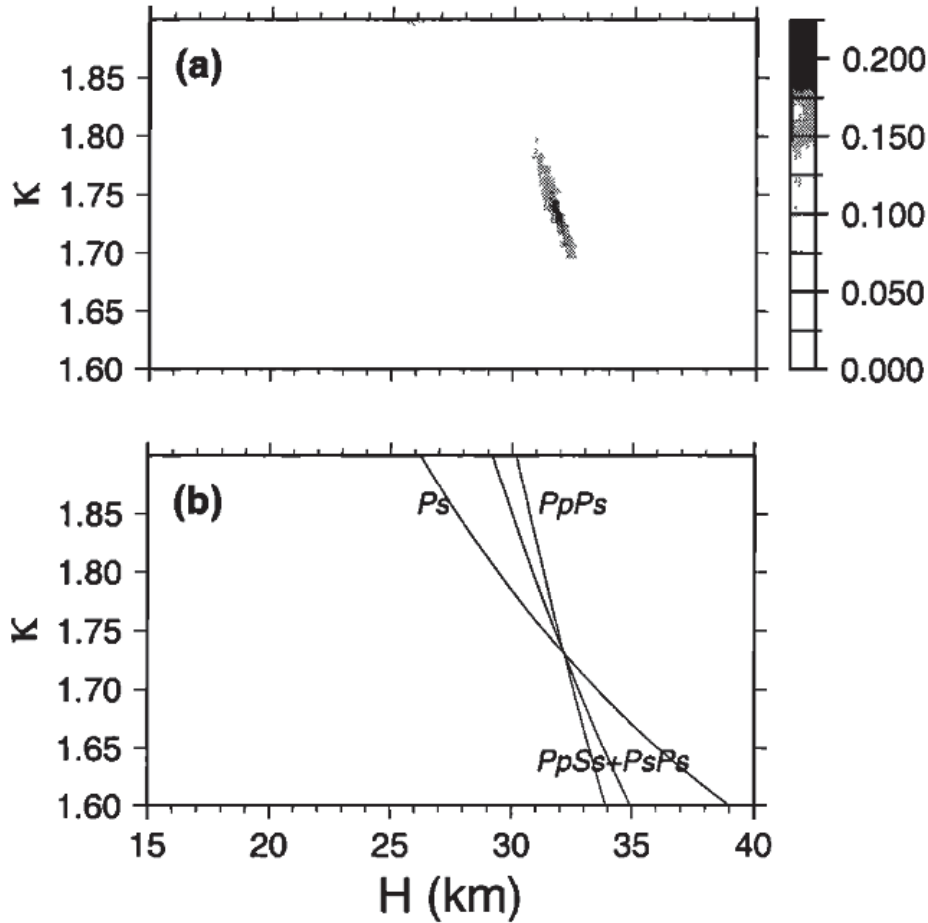


Figure 2.3: (a) The  $s(H, \kappa)$  from stacking the receiver functions in Fig. 2.2. It reaches the maximum (solid area) when the correct crustal thickness and  $V_p/V_s$  ratio are used in the stacking. (b)  $H-\kappa$  relations for different Moho converted phases in Fig. 2.2. Each curve represents the contribution from this converted phase to the stacking. (from Zhu and Kanamori [2000, P.2972])

## 2.3 CCP stacking

The common-conversion-point(CCP) stacking method is usually applied to generate a high resolution image when closely-spaced stations are available. The idea for this method [Zhu, 2000] is to transfer RFs from the time-domain to depth-domain. First, we need to calculate the ray-paths of the receiver functions using a background velocity model. After being corrected for the incident angle effect, the amplitude at each point on the receiver function is assigned to the corresponding location on the ray-path. The location is determined by using its time delay with respect to the direct  $P$ , based on the  $V_p/V_s$  ratio determined by the H- $\kappa$  stacking method. Then the volume along the profile is divided into certain size bins and all amplitudes in each bin where the ray goes through are stacked to obtain the average amplitude and variance. For example, a CCP stacking image in Zhu [2000] has bin size of 30 km wide, 10 km long, and 0.5 km high. Neighboring bins overlap by 9 km along the profile to smooth the 2-D image(Fig. 2.4). The quality of the image depends on how many RFs passed through each bin. Data from as many stations and events as possible were collected to improve the resolution of images.

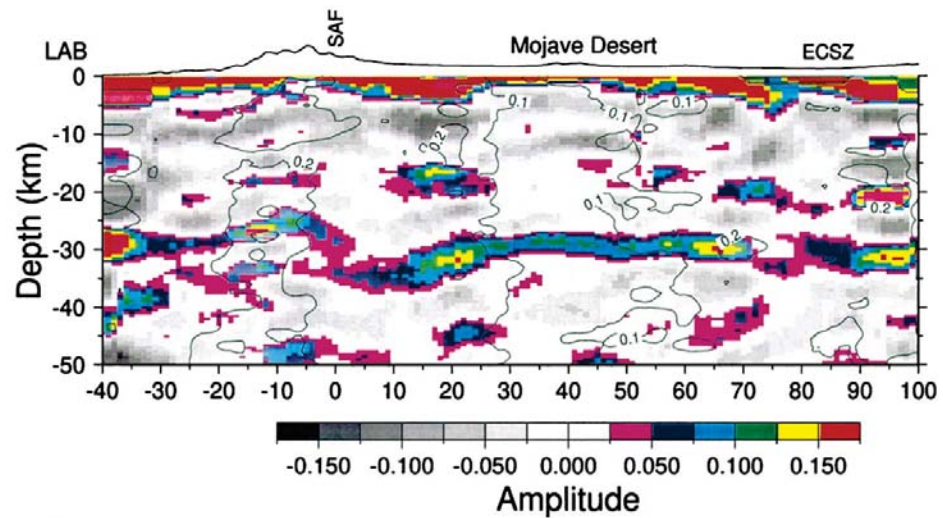


Figure 2.4: Amplitude and variance (given by the contours) of CCP stacking for a profile across the San Andreas Fault in southern California. No vertical exaggeration except that the surface topography is amplified by a factor of 2. (from Zhu [2000, P.186])

## Chapter 3: Crustal Structural Variation of the Southern and Central Tibetan Plateau from Teleseismic Receiver Function Studies

### 3.1 Introduction

The Tibetan Plateau, the Earth's highest and largest plateau, was generated by the collision between the Indian and Asian plates. High-resolution digital topography shows a relief of 1 km or less for most of the area of Tibet except at the plateau edges [Fielding *et al.*, 1994]. The plateau is bounded by India to the south. Two major sutures divide several terranes. From India to central Tibet, they are Yarlung-Zangpo Suture (YZS), the Lhasa Terrane, the Bangong-Nujiang Suture (BNS), and the Qiangtang Terrane (Fig. 3.1).

The Tibetan Plateau is composed of continental fragments that were added successively to the Eurasian plate. The sutures between these microplates are characterized by the presence of ophiolitic material. The BNS formed during the late Triassic-early Jurassic and separates the Qiangtang Terrane from Lhasa Terrane. The YZS was the latest suture to form from the collision of the Indian plate and the Lhasa Terrane in the early Tertiary [Dewey *et al.*, 1988]. The closure of the Tethys ocean in the early Cenozoic Era brought the Indian continent in contact with Eurasia. India has continued to move northward into Eurasia. The development of the Cenozoic Tibetan plateau began in the Eocene about 50–40 Ma [Patriat and Achache, 1984]. A total of about 1400 km N-S convergence has occurred between India and the interior of Eurasia since the beginning of the collision [Yin and Harrison, 2000]. The uplift of the plateau began in the middle Eocene (45 Ma) [Patriat and Achache, 1984], and accelerated at 8 Ma [Molnar *et al.*, 1993]. This uplift elevated the Tibetan Plateau to be the "Roof of the world" on top of an anomalously thick crust of 70–90 km [Mejia, 2001].

So far, several end-member models have been proposed for the India-Asia

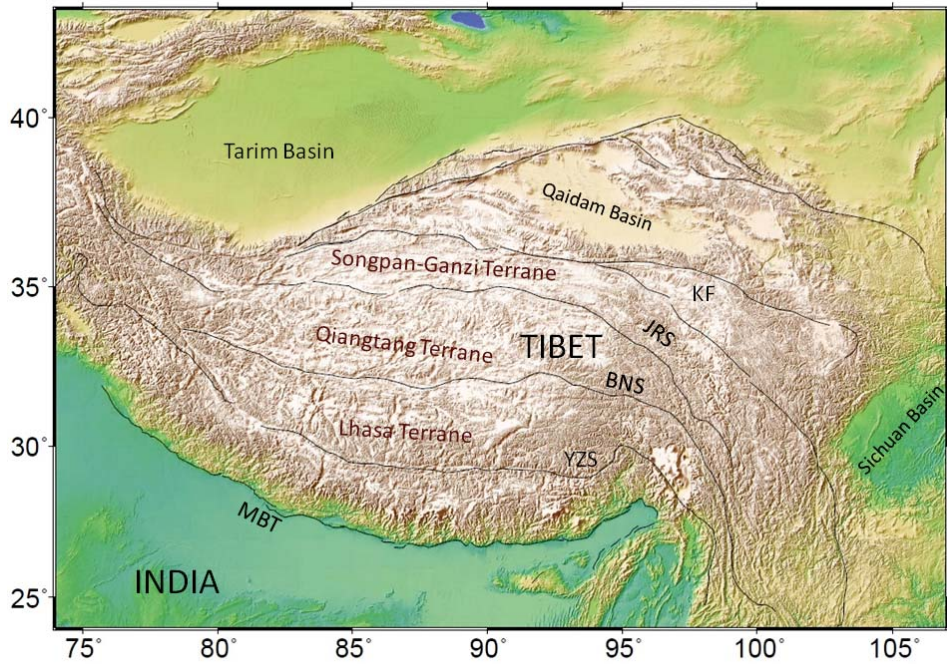


Figure 3.1: Map of the Tibetan Plateau and surrounding areas. MBT: the Main Boundary Thrust; YZS: the Yarlung-Zangbo suture; BNS: the Bangong-Nujiang suture; JRS: the Jinsha River suture.

collision and uplift of the Tibetan Plateau. An early model by *Ni and Barazangi* [1984] suggests that the Indian plate underthrusts beneath the Asian crust to form the thick Tibetan crust. This model predicts a progressive south-to-north uplift of the plateau, which is however in conflict with the observed synchronous uplift history [Wu, 1983]. A later model by *Zhao and Morgan* [1985] was developed where the Indian crust is injected into a weaker Tibetan lower crust. Thus the plateau is raised uniformly in a manner similar to a piston in a hydraulic jack. These two models do not address the question of what happened to the Asian mantle lithosphere displaced by the underthrust India lithosphere (the underthrust model) or the Indian mantle lithosphere (the injection model). Both require more than 1000 km of underthrusting or injection of Indian crust, which is at odds with the estimated Indian crust shortening of less than 400 km based on the restoration of all

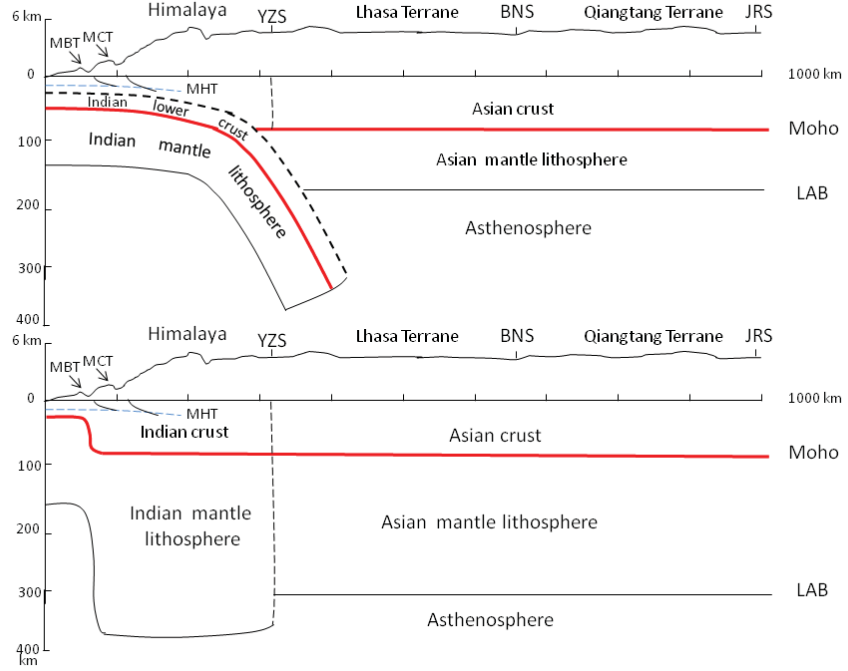


Figure 3.2: The upper cartoon shows the India lower crust and mantle lithosphere subducting beneath YZS; The lower cartoon shows the Indian plate shortening horizontally and thickening vertically. The red thick lines represent the Moho. MHT: Main Himalaya Thrust. MCT: Main Central Thrust. LAB: Lithosphere Asthenosphere Boundary.

reverse faults between MBT (the Main Boundary Thrust) and YZS (the Yarlung-Zangbo suture) [Hauck *et al.*, 1998]. The distributed shortening model by Dewey *et al.* [1988]; England and Houseman [1988] suggests that the N-S convergence is largely accommodated by horizontal shortening and vertical thickening of Asian crust and mantle lithosphere. A delamination or thermal erosion of a large portion of the thickened Asian lithosphere was also suggested in the model to explain the rapid uplift to 5 km elevation since 8 Ma. Several recent models [Tilmann *et al.*, 2003] put the Indian mantle lithosphere underthrusting beneath southern Tibet and subducting near the BNS.

How such convergence is accommodated in a continent-continent collision and how such a high plateau was formed has been a focus of international geological and

geophysical research since the 1970s. Most of the previous studies about Indian-Asian collision models focused on crustal interactions and the subsequent uplifting of the Tibetan Plateau. For oceanic-oceanic or oceanic-continental plate collision, the convergence always occurs in the form of subduction of an oceanic plate as a result of the negative buoyancy associated with the oceanic lithosphere. The continental crust, on the other hand, is usually thick and consists of low density rocks and a depleted mantle lithosphere of neutral buoyancy [McKenzie, 1969]. It is therefore questionable whether a significant amount of continental lithosphere can be subducted. Thus knowing the ultimate fate of the Indian mantle lithosphere will help us to understand plate tectonics processes for continent-continent interactions, and will help develop accurate collision models.

The Moho is the most prominent discontinuity which separates the crust from the mantle, and its location can provide important constraints on mantle lithosphere deformation. As shown in Fig. 3.2, if the Indian lithosphere subducts beneath the YZS or further north, the Indian Moho will have a northward dip beneath the Himalayas. If the Indian lithosphere does not subduct and is shortened beneath the Himalayas, the Moho will be flat and one should expect a vertical offset of the Moho beneath the MBT.

Seismologists made their contribution to define the structures beneath this region. In particular, the teleseismic receiver function method is an effective way to find an interface that has a velocity contrast and can be used to determine crustal thickness and variations. Wittlinger *et al.* [2009] combined *S*-to-*P* and *P*-to-*S* receiver function methods and found that the crustal thickness beneath the Lhasa terrane is approximately 75-78 km, and that the Qiangtang terrane's Moho is at 70 km depth. Because of the high shear-wave velocities and low Vp/Vs ratio, they proposed that the deep Indian lower crust underplated beneath Tibet has turned to eclogite, and extend northwards only to the middle of the Lhasa terrane. Mitra

*et al.* [2005], using the same method proposed that the Indian crust and upper mantle lithosphere were underthrust beneath Himalaya and southern Tibet. Instead of using the receiver function method, *Tseng et al.* [2009] used waveform modeling(SsPmP vs Ss) while *Nowack et al.* [2010] used Gaussian-beam migration of scattered teleseismic *P*-wave to image the crust and upper mantle beneath Tibet. Both of these studies showed a northward thinning crust, from  $\sim$ 75 km thickness in southern Tibet to just over  $\sim$ 60 km thick under the Qiangtang terrane, and a disrupted Moho beneath the BNS. The *P*-wave wide-angle reflection or refraction method was used by *Zhao et al.* [2001], who determined that crustal thickness is 70–80 km in the southern Lhasa terrane and 60–70 km in the northern part of the Lhasa terrane and Qiangtang terrane. *Haines et al.* [2003] also used this method to find a weak Moho beneath the BNS and shallow low velocity layers which suggested a lateral escape of the lower crust.

In this study, all the available teleseismic data before 2005 were collected and processed. Teleseismic receiver function methods were used to determine crustal structural variation of most of the southern and central Tibetan plateau. Data sets from more than 300 stations were used to compute receiver functions (RFs) and determine crustal thickness and Vp/Vs ratio beneath each individual station with the H- $\kappa$  stacking technique [*Zhu and Kanamori*, 2000]. High resolution images of the crust and uppermost mantle were obtained using the CCP stacking method [*Zhu*, 2000] for several profiles where station spacings are small. Finally an interpretation of the most broad area of the collision zone based on the receiver functions' studies is presented based on all results.

### 3.2 Data

Teleseismic *P*-wave data from the 2002-2005 Hi-Climb array [*Nabelek et al.*, 2009], the 1994-1999 INDEPTH II and III array [*Brown et al.*, 1996], the 2003-2004

Namche Barwa Tibet array [Sol *et al.*, 2007] and the 2001-2002 Himalayan Nepal Tibet Experiment array [Schulte-Pelkum *et al.*, 2005] were collected and processed. In total, there were 322 broadband seismic stations deployed across the High Himalayas, southern and central Tibet Plateau, 182 stations from the Hi-Climb array, 60 stations from the INDEPTH array, 51 stations from the Namche Barwa Tibet array and 29 stations from the Himalayan Nepal Tibet Experiment array (Fig. 3.3). A 0.05-2.0 Hz band-pass filter was applied to all seismograms. Only events having magnitudes larger than 5 were used. After visual inspection, more than 4000 teleseismic events with clear *P*-wave signals were used. For each event, I aligned the *P* waveforms from all the stations on the first *P* arrival time using an automatic multi-station waveform cross-correlation algorithm. Fig. 3.5 shows an example of inspected *P*-wave records of an earthquake. After the cross-correlation, bad records were identified and deleted automatically. This allows for accurate selection of the first *P* arrival time and deletion of noisy recordings. The Hi-Climb array recorded 2082 events, the INDEPTH array recorded 843 events, the Namche Barwa Tibet array recorded 770 events, and the Himalayan Nepal Tibet Experiment array recorded 456 events. In Fig. 3.4, four arrays are plotted in the center of the figures respectively. All the events distributed between 30° and 90° away from the stations. Most of events are located to the east and south. Fewer events are located to the north and west. Finally, I obtained 52,692 RFs of Hi-Climb array, 7555 RFs from INDEPTH array, 6892 RFs of Namche Barwa Tibet array and 1795 RFs from the Himalayan Nepal Tibet Experiment array.

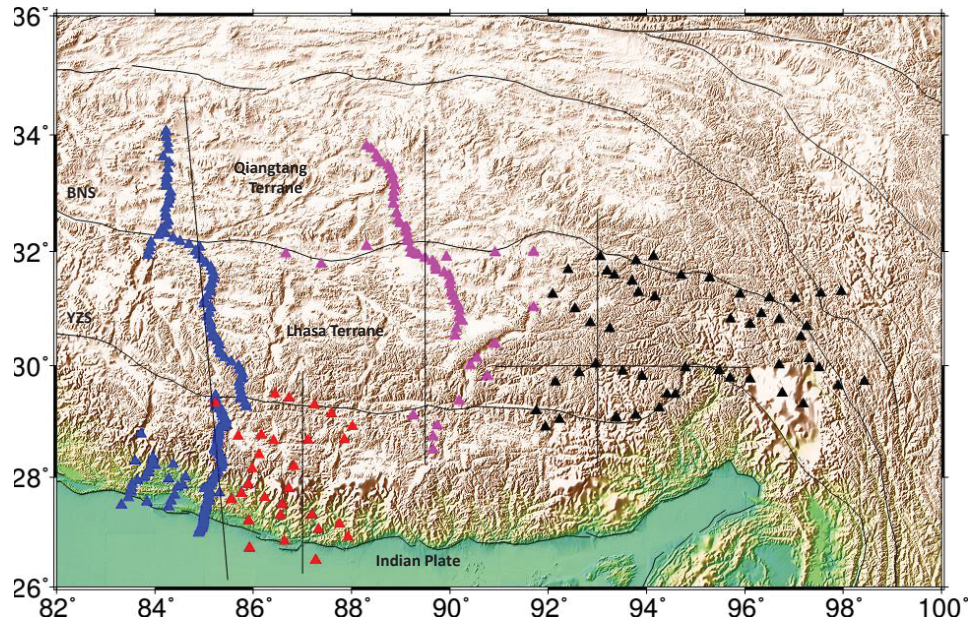


Figure 3.3: Locations of 322 stations from the four projects used in this study (Blue triangles show the HiClimb array, magenta triangles the INDEPTH I & II array, red triangles the Himalayan Nepal Tibet Experiment array and black triangles the Namche Barwa Tibet array). BNS stands for Bangong-Nujiang Suture. YZS stands for Yarlung-Zangbo Suture. The black lines are the CCP imaging profiles of each array.

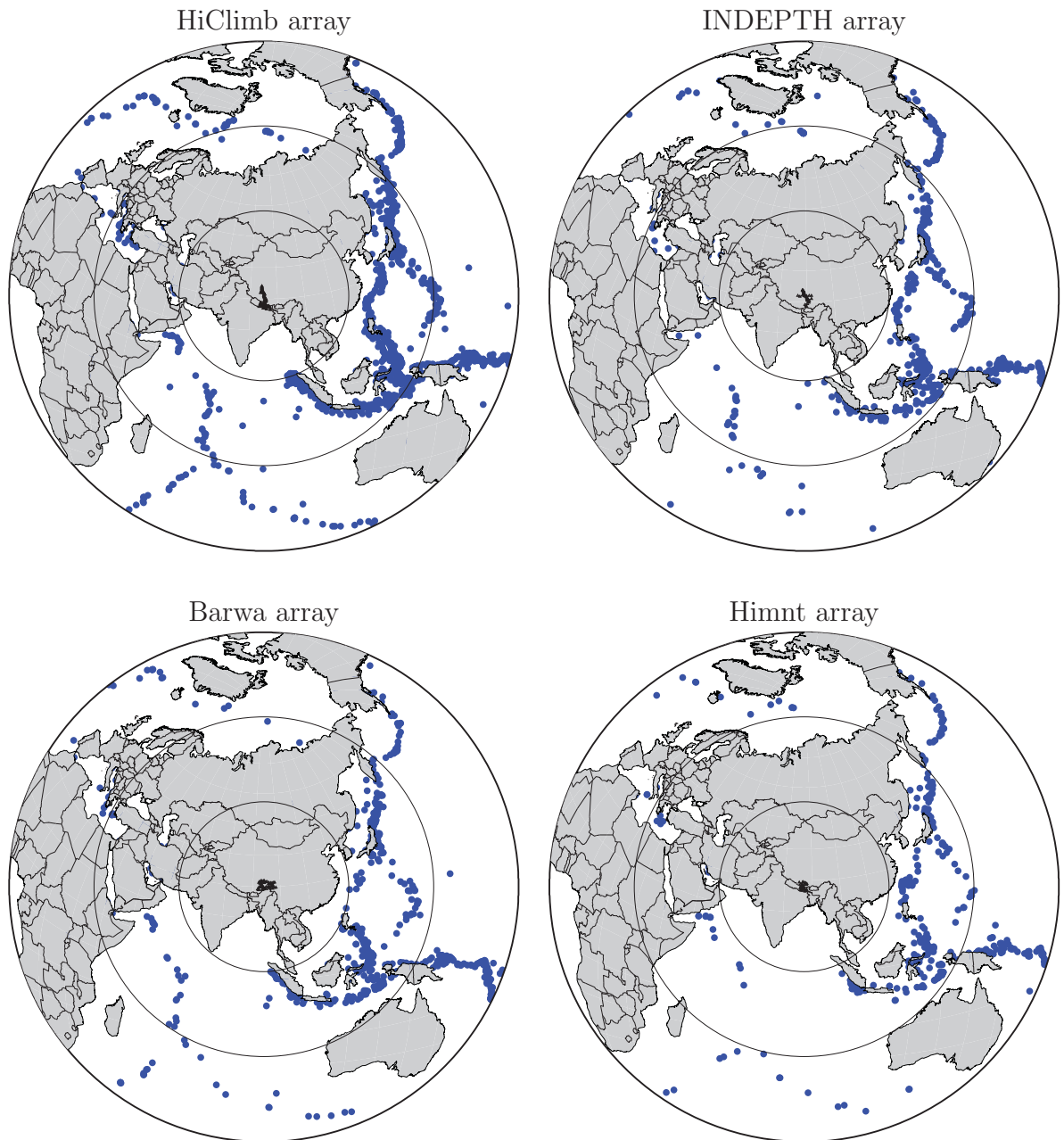


Figure 3.4: Locations of broadband stations of the four arrays are shown as black triangles. The blue circles are the selected events recorded by the arrays.

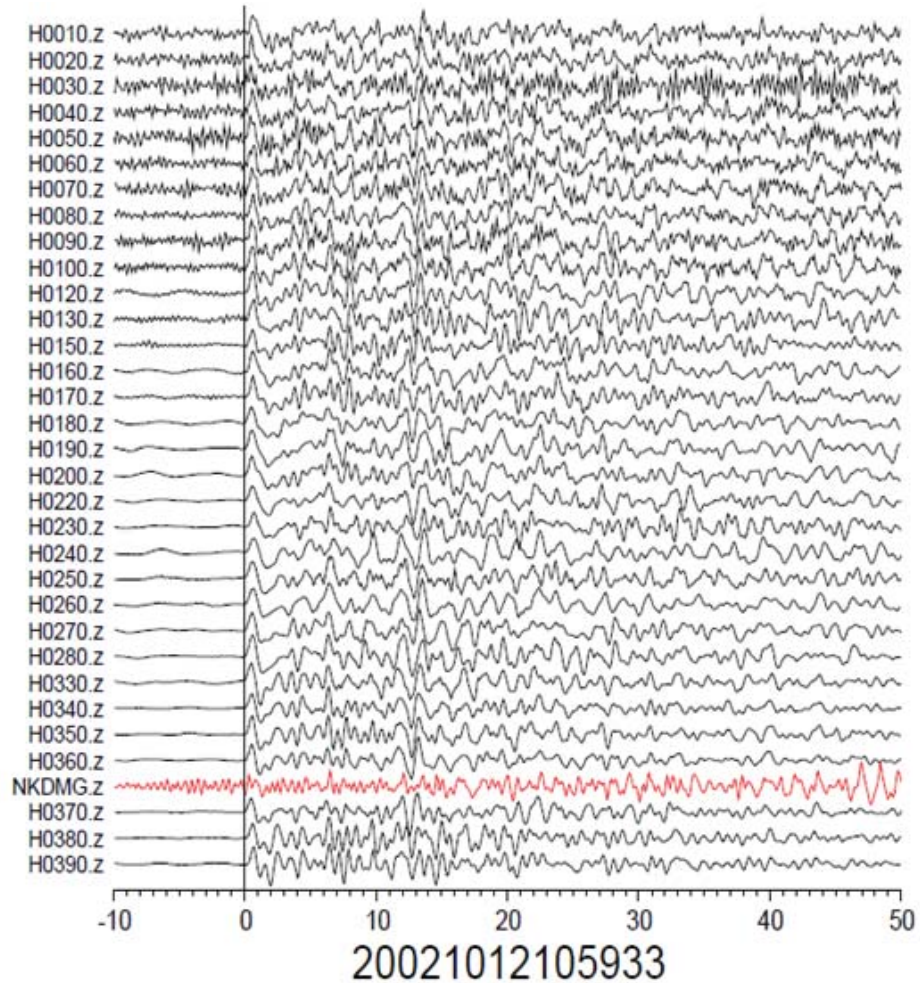


Figure 3.5:  $P$ -wave records from an earthquake on October 12, 2002. The vertical black line aligns the first  $P$ -wave arrival times at all stations from the Hi-Climb array. The red trace is a bad record identified automatically by the multi-station waveform cross-correlation processing.

### 3.3 Results

#### 3.3.1 H- $\kappa$ stacking results

The H- $\kappa$  stacking method was applied to all the stations of the four arrays. Only the H and  $\kappa$  results which clearly indicate the  $Ps$ ,  $PpPs$  and  $PsPs + PpSs$  phases were kept. The maximum value of the H- $\kappa$  stacking has to fall within a reasonable range. In this case, the crustal thickness is from 50-90 km with  $\kappa$  value from 1.5-1.9.

For the Hi-Climb array the H- $\kappa$  stacking method was applied to all 182 stations resulting in reliable Vp/Vs ratios for 57 stations shown in Fig. 3.6. Low Vp/Vs ratios are distributed south of YZS (Indian Block). The Lhasa terrane and middle Qiangtang terrane's Vp/Vs ratio is not as consistant with  $\kappa$  values varying from 1.60 to 2.00.

Most of the stations of the Himalayan Nepal Tibet Experiment array have lower than average Vp/Vs ratios (1.732) in this region [Tian *et al.*, 2005]. Even though some stations located west of this area have  $\kappa$  values close to 1.75, the majority of the stations have Vp/Vs ratios between 1.5 and 1.7.

For the INDEPTH array, the H- $\kappa$  stacking method was applied to all 60 stations. The resulting Vp/Vs ratios are shown in the middle of Fig. 3.6. There are no consistant  $\kappa$  values in this area, except for the stations within the rift systems, which is different from the Himalayan Nepal Tibet Experiment array. The rift systems are discussed in the next chapter. The Vp/Vs ratio results are different from the previous results of Tian *et al.* [2005]. Even though I used the same method, I collected all the available teleseismic  $P$ -waves to calculate the  $\kappa$  values and found that the Vp/Vs ratios in this area are not as consistently high as they found. Fig. 3.6 illustrates that the high Vp/Vs ratios and low Vp/Vs ratios are randomly distributed. The Vp/Vs ratio value varies from 1.6 to 1.9.

The Namche Barwa Tibet array results are shown in the eastern portion of the

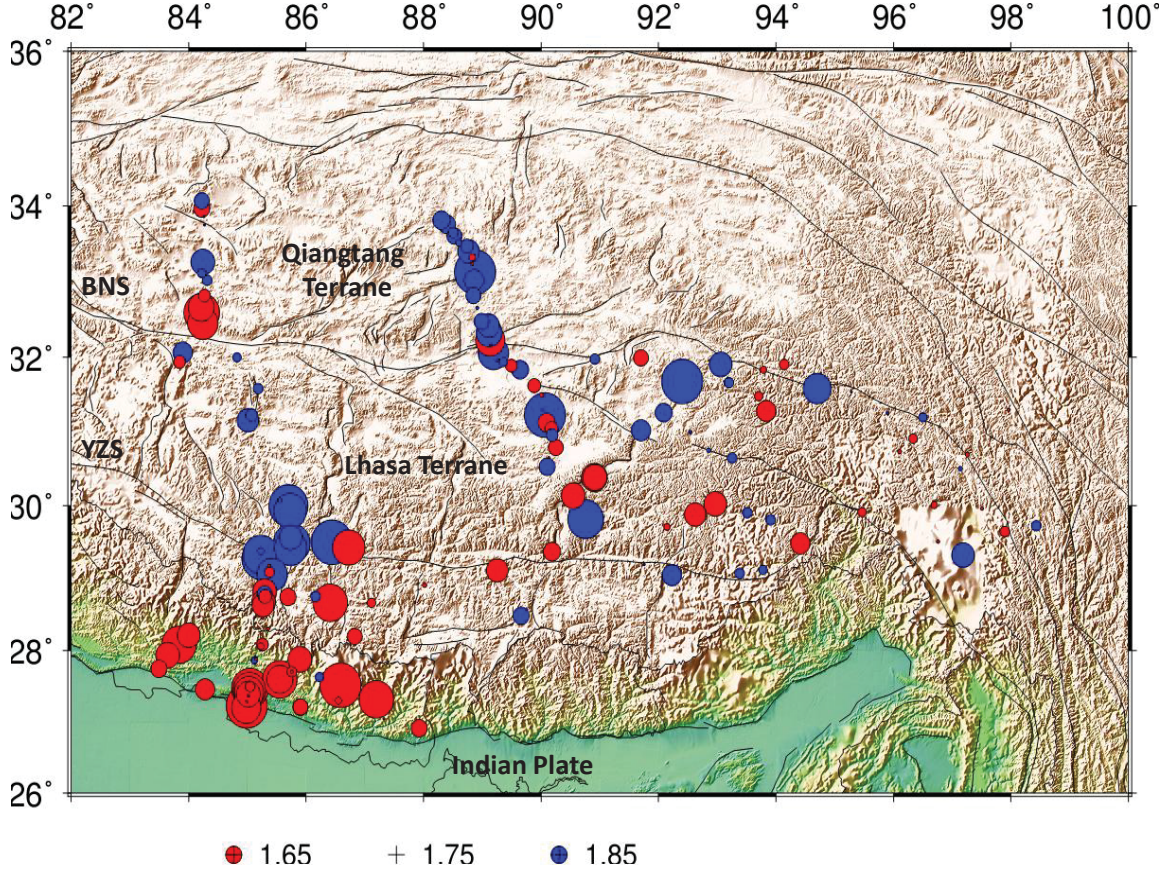


Figure 3.6: The  $V_p/V_s$  ratios are shown in colored circles. Blue means higher than the average value. Red means lower than the average  $V_p/V_s$  ratio.

Fig. 3.6. The  $\kappa$  values are higher than 1.80 in the western region of this array. In the eastern part, the  $\kappa$ 's values are close to the normal range around 1.75.

### 3.3.2 CCP stacking results

I obtained CCP stack results based on the receiver functions and  $\kappa$  values determined by the H- $\kappa$  stacking method, to image detailed crustal structure across the study area. The 1-D velocity model, used to convert the receiver functions from time-domain to depth-domain, is a modified Tibet model by Zhu (2003). The  $V_p/V_s$  ratio of the original model was substituted by the  $\kappa$  values determined by the H- $\kappa$  stacking technique. The width of the stacking profile was set to 300 km in order to

utilize all the RFs collected by the stations. The stacking bin size is 1 km along the profile, 100 km perpendicular to the profile, and 0.5 km in depth.

I obtained four north-south trending crustal images, which are shown in Fig. 3.7, down to 150 km using the CCP stacking method to detect Moho variations and intra-crustal interfaces along the profiles. The 950 km long Hi-Climb CCP profile is shown in Fig. 3.3. This profile is oriented NNW-SSE crossing the southern Qiangtang Terrane, the Lhasa Terrane and Himalayas. In the image (Top of Fig. 3.7), there are two positive amplitude interfaces beneath this array. A north dipping interface starts at 40 km depth south of MBT and stops nearly 50 km depth beneath south of the YZS. The other interface starts just beneath the northern end of previous interface at 80 km south of YZS. It extends horizontally northward to the center of the Lhasa terrane at about 60 km depth. The interface beneath the YZS is continuous, smooth and strong. The Moho beneath BNS and nearby area is weak. Further north of BNS, the Moho is visible at 58-60 km depth.

The crustal image of Himalayan Nepal Tibet Experiment array is obtained by CCP stacking along the profile shown in Fig. 3.3. This profile is near the HiClimb array which is oriented north to south. Since the Himalayan Nepal Tibet Experiment array only covers the region of YZS and its southern area, the CCP images can only show the crustal structures south of the YZS. The second image in Fig. 3.7 shows two interfaces beneath northern India and Himalaya that are both dipping to the north. The upper interface begins at 20 km depth beneath MBT, and intersects the lower interface at YZS. The lower interface is about 20 km deeper than the upper interface and extends to about 60 km depth beneath the YZS.

To compute a high resolution CCP image of INDEPTH array, I used the INDEPTH profile shown in Fig. 3.3, which is oriented north-south passing through from the center of Qiangtang terrane to Himalayas. In the high resolution crustal image shown in the third image of Fig. 3.7, the Moho depth increases from 60 km in

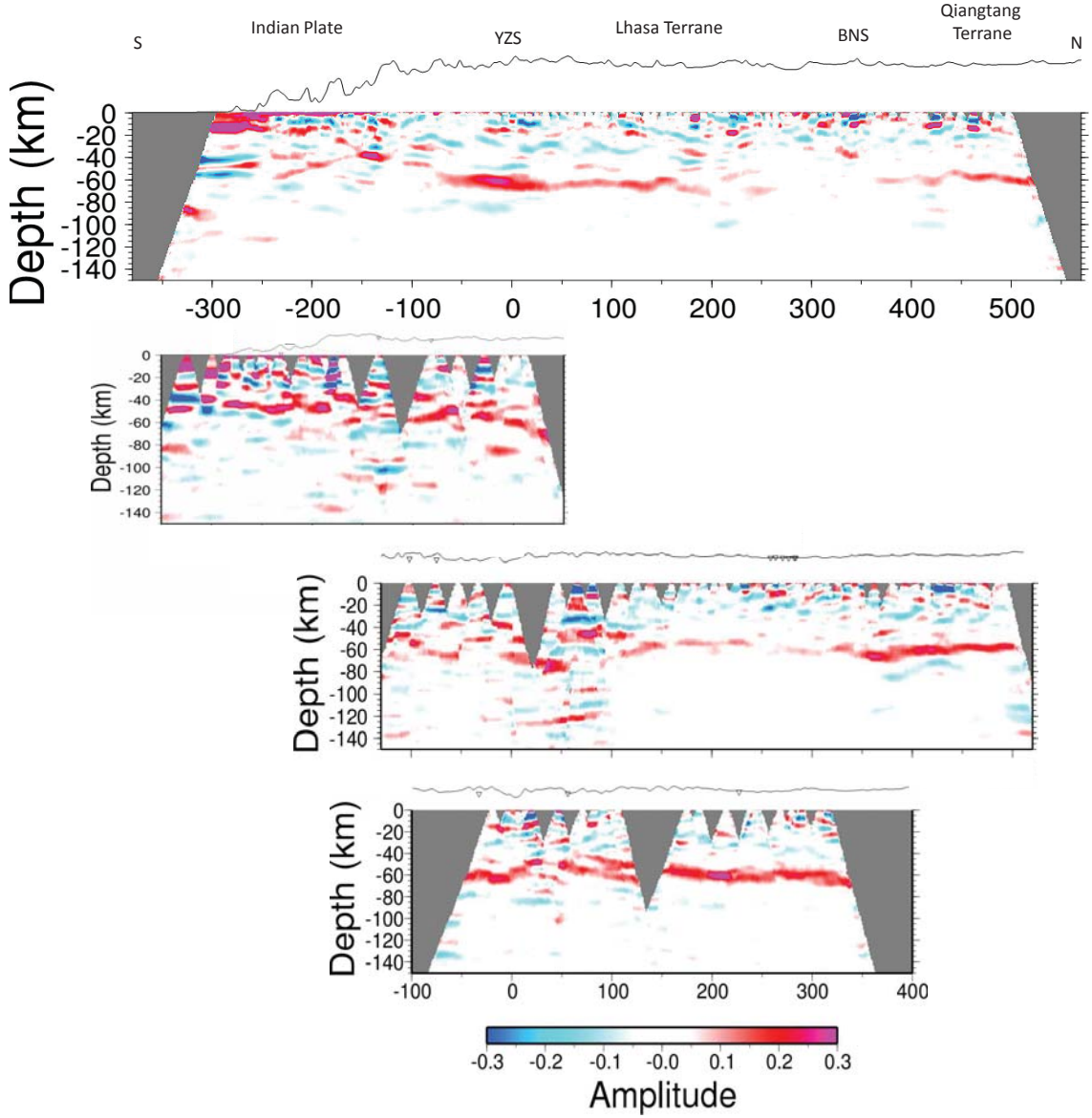


Figure 3.7: CCP stacking images along profiles shown in Black lines in Fig. 3.3. From the top to bottom, the images are from the Hi-Climb array, INDEPTH II and III array, Himalayan Nepal Tibet Experiment array, and Namche Barwa Tibet array, respectively. Amplitude shows the vertical velocity change. Positive value means velocity increase downward. Negative value means the opposite. All these images are aligned with the surface trace of YZS, which is marked 0 km on the horizontal axis.

the Lhasa block to about 70 km in the Qiangtang block. This is different from the results of *Tseng et al.* [2009], *Wittlinger et al.* [2009] and *Nowack et al.* [2010]. This study uses a more extensive data set, so I consider my results to be more robust.

Another interesting feature is an interface dipping towards the north from  $28^{\circ}$  N, starting at 45 km depth, extending to 70 km depth beneath the YZS, and terminating near 100 km north of YZS at 80 km depth. A clear discontinuity near Moho depth is between 60 and 100 km north of YZS. Compared with the HiClimb array, the Moho beneath BNS is stronger. The Moho lies at near 60 km depth beneath the BNS. There is no other obvious discontinuity near this area.

The Namche Barwa Tibet array's CCP image is shown at the bottom of Fig. 3.7. This profile crosses BNS and YZS and oriented North-South. Due to the sparse stations in the east, only one CCP image between  $92^{\circ}$  E and  $94^{\circ}$  E was obtained. The most distinct feature is the double interface north of YZS. The upper interface is simple and is clearly dipping towards north. This interface starts from 50 km north of the YZS at 45 km depth, extending northwards and dipping until 200 km north of the YZS. Further north, the Moho extends relatively flatly at 60 km depth, and starts to dip to about 70 km depth at BNS. Since the interface goes deeper towards the Qiangtang Terrane, the crustal thickness of the Qiangtang Terrane might be larger than 70 km. The lower interface has an irregular shape, and is more complex than the upper interface. First, it dips to about 70 km beneath YZS, and then bends upward to about 50 km depth at north of the YZS, and finally dips northwards again and terminates at 70 km depth near 120 km north of the YZS. These two interfaces are parallel to each other between 70 km and 120 km north of the YZS. The separation between them is about 15 km. Another profile in this area is shown in Fig. 3.8, which is along the east-west direction shown in Fig. 3.3. I generated this CCP image because some of the crustal anomalies and irregular shaped interfaces shown in the CCP image along the previous north-south profile of Namche Barwa Tibet array. I adjusted the bin size to exclude the receiver functions 30 km away from this profile, for the reason that the crustal variations are large along the north-south direction. In this Figure, two interfaces near the  $93^{\circ}$ E are

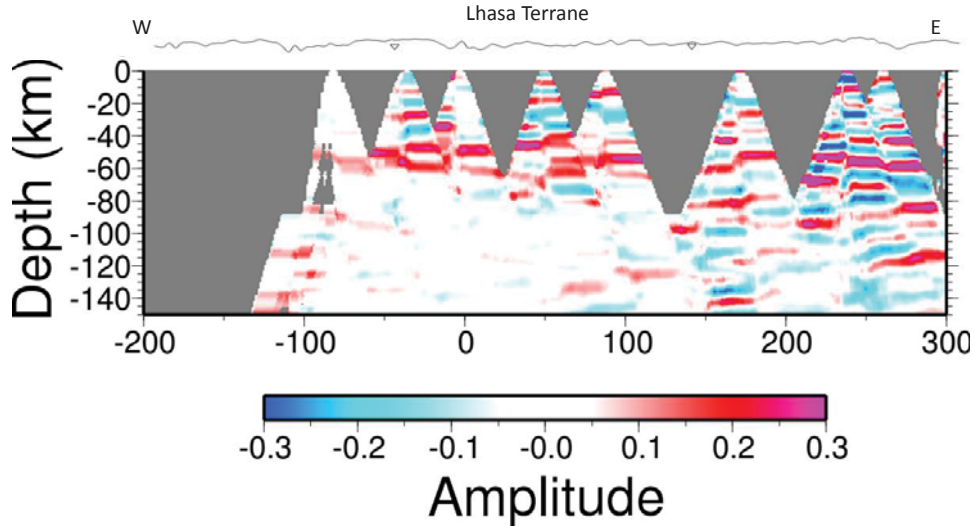


Figure 3.8: CCP image along an east-west profile, centered at 93°E, 30°N.

observed. The upper interface is at 50 km depth. The lower one is at about 60 km depth. These two interfaces correspond with those in the north-south oriented CCP image.

### 3.4 Discussion

#### 3.4.1 Collision model

*Kind et al.* [2002] used teleseismic  $P$ -wave receiver functions to obtain an image of crustal and upper mantle interfaces beneath Tibet but did not find the Indian subducting slab. They interpreted their results in terms of detachment of the Indian oceanic lithosphere. However,  $S$ -wave receiver functions, which are more sensitive to upper mantle interfaces, indicate that the Indian lithosphere subducts northward from a depth of 160 km beneath the Himalayas to a depth of 220 km just south of the Bangong-Nujiang Suture [*Kumar et al.*, 2006]. *Tilmann et al.* [2003] obtained a  $P$ -velocity structure along the INDEPTH III line by inversion of  $P$ -wave travel times. They found a subvertical high velocity zone from  $\sim$ 100 to  $\sim$ 400 km depth south of the BNS. They interpreted these results as subducted Indian mantle

lithosphere. *Xie et al.* [2004] observed extremely low  $Lg Q_0$  in the southern Tibetan Plateau, and interpreted it as being caused by partially molten middle crust. Thus they inferred that the Indian lithosphere underthrust beneath the Lhasa terrane because their results were consistent with the underthrusting condition.

*Jimenez-Munt et al.* [2007] constructed a two-dimensional lithospheric thermal and density model crossing the Himalaya front and the Tibetan Plateau. This model is based on the assumption of local isostatic equilibrium and is constrained by the topography, gravity and geoid anomalies and thermal data in the crust. They suggested that the convergence between the Indian and Asian plates put the Indian lithosphere beneath the Tibetan Plateau and part of the thickened lithospheric mantle south of the BNS has been removed. The lithosphere extends to 260 km depth beneath southern Tibet, but 100 km under central and northern Tibet. 3D variations of  $P$  and  $S$ -wave speeds beneath Tibet were obtained by *Huang et al.* [2010] using multi-scale, finite-frequency travel time tomography. They concluded that the subhorizontal subducting Indian lithosphere stopped at  $\sim 33^\circ$  N, and then extruded in the eastward direction.

My receiver function results indicate that the Indian mantle lithosphere subducted between  $85^\circ$  E to  $93^\circ$  E (Fig. 3.7). Northern dipping Moho of the Indian plate is shown in the four arrays. These results suggest that in continent-continent collision, a continental mantle lithosphere can subduct. The Moho near the MBT dips towards the north, without the Moho offset predicted by the horizontal shortening model (Fig. 3.2).

Another interesting result is the along-strike variation of location and depth of the Indian subduction front. In the west along the HiClimb profile ( $85^\circ$ E), the subduction front at the Moho depth is about 100 km south of the YZS. In the east along the Barwa profile ( $93^\circ$ E), the subduction front at the Moho depth is 100 km north of the YZS (Fig. 3.9). In addition to this misalignment between the plate

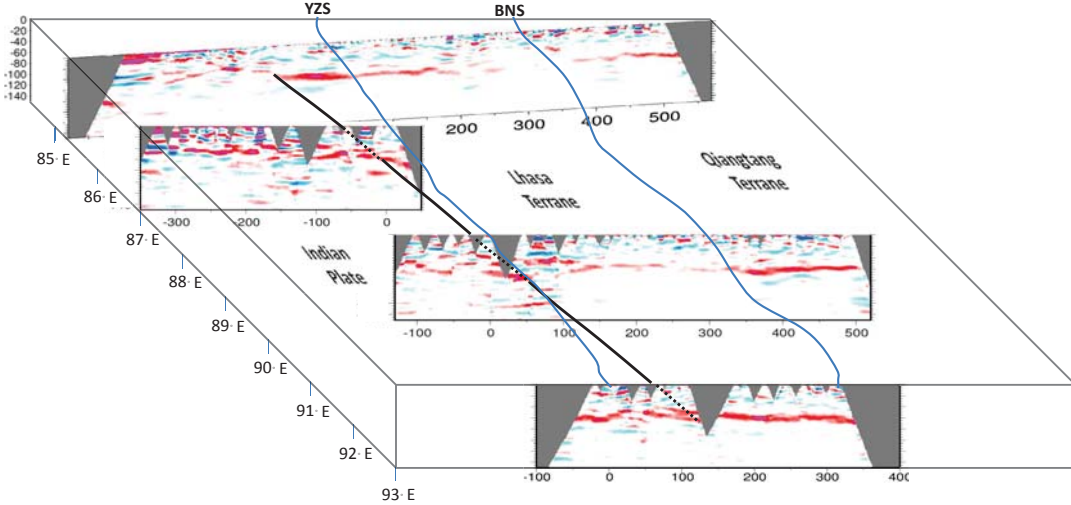


Figure 3.9: Illustration of the oblique subduction of the Indian mantle lithosphere. The black line is the India-Asia plate boundary at the Moho level. The two blue lines are the surface boundary of YZS and BNS.

boundary at the surface (Yarlung-Zangpo Suture) and at the bottom of the crust, the top of the subducting Indian slab also varies from west to east (Fig. 3.10). It reaches the maximum depth (75 km) under the INDEPTH array profile and becomes shallower (60 km) under the HiClimb and Barwa profiles. These along-strike variations demonstrate the 3D feature of the India-Eurasia continental collision.

The CCP images along profiles of east-west and north-south directions in Fig. 3.7 and Fig. 3.8, show double Mohos near 93°E and 30°N, about 100 km north of the YZS. Based on the observations, I suggest that the Indian mantle lithosphere underthrusts underneath the Tibetan Plateau's crust, thus generates two large velocity contrast interfaces which are detected by the receiver function methods.

For the uplifted Moho beneath the YZS in this region, there are no previous observations about this structure. My explanation would be hot mantle materials upwelling and bending the Indian crust. Another possibility is the delamination of eclogite from the bottom of the Indian crust.

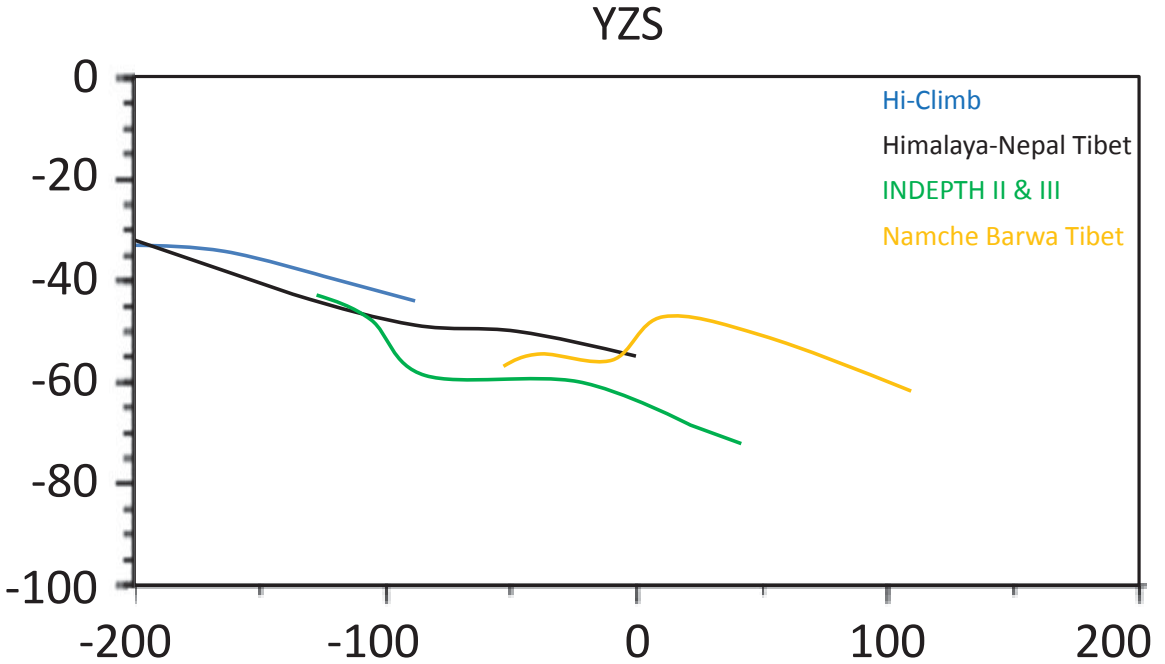


Figure 3.10: The Moho images of Indian mantle lithosphere from four arrays' receiver function results. Each color represents one array. These images are centered at YZS and show the Moho variation to a distance of 200 km north and south of the YZS.

### 3.4.2 Crustal structure beneath the BNS

In the central part of the Tibetan Plateau, the BNS is the boundary between the Qiangtang terrane and Lhasa terrane. This suture was closed during the late Jurassic-early Cretaceous based on geological survey. Whether the suture is just a surface feature or extends to the lower crust and upper mantle , is an interesting problem.

Based on the INDEPTH III data analysis, *Haines et al.* [2003] found no low velocity structure beneath BNS, and suggested that the suture doesn't reach the lower crust. *Tian et al.* [2005] proposed that the Moho is separated near BNS based on a joint imaging of receiver functions. *Nowack et al.* [2010] applied Gaussian-Beam migration method to Hi-CLIMB array data, and found there is over

200 km in length of disrupted Moho beneath BNS.

The CCP images from HiClimb, INDEPTH and Namche-Barwa arrays, show that the Moho beneath BNS varies from west to east (Fig. 3.9). The CCP image of HiClimb array does not show clear Moho beneath BNS. However, to the east, the Moho is clear and simple beneath BNS. The CCP images from INDEPTH and Namche-Barwa arrays show that the Moho is at the depth of about 60 km beneath Lhasa terrane, and increases to about 70 km under Qiangtang Terrane. However, no obvious Moho discontinuity or offset is observed near BNS.

### 3.4.3 Partial melting in the southern and central Tibet

Two opposite views exist about properties of the lower crust in southern Tibet. The first view is that the middle or lower Tibetan crust is partially molten based on the low velocity zone detected by seismic methods [Brown *et al.*, 1996; Makovsky *et al.*, 1996; Alsdorf *et al.*, 1998; Li *et al.*, 2003]. Other people argued that the middle or lower crust is strong and coupled with upper crust in lithosphere deformation [Yin, 2000; Kapp *et al.*, 2005; Copley *et al.*, 2011]. Kapp *et al.* [2005] applied geochemical analyses and surface observation to exhumed mid-crust exposures of Nyainqntanglha(NQTL) Shan, in the northern part of the Yadong-Gulu rift. The thermochronologic studies of footwall K-feldspars indicate little perturbation of background thermal structure, which combined with undeformed footwall and the lack of migmatites exposed in the NQTL, indicated the partial melt zone did not exist or at least in the youngest magmatic episode of this region. To the central part of the plateau, Haines *et al.* [2003] used reflection and refraction methods and found that there is no evidence of 'bright spot' in central Tibet from INDEPTH III data, which means partial melting is limited in southern Tibet. Tian *et al.* [2005] applied receiver function methods to the same data from INDEPTH III array, obtained higher than normal Vp/Vs ratio 1.81

beneath central Tibet. Based on the results, they proposed a wide-spread partial melting in this region. To the west, *Nabelek et al.* [2009] used similar methods to calculate receiver functions from the Hi-CLIMB project, also determine the crustal  $V_p/V_s$  ratio across southern and central Tibet. They found a low  $V_p/V_s$  ratio in this region, which argues that there is no partial melting to the west. *Xu et al.* [2011] used S-receiver functions method and detected low velocity layer between 20-40 km depth. This mid-crustal low velocity layer extends along the entire profile, but is distributed discontinuously. *Wittlinger et al.* [2009] applied H- $\kappa$  stacking method to the same region, based on the linear relationship between  $V_p/V_s$  ratio and  $S$  wave velocity. They found out that the deficit of crustal thickening is related with vertical mass transfer and concluded that there is 19 km eclogite in the bottom of crust north of YZS.

*Zhao and Morgan* [1985] suggested that Indian crust injects into a weaker Tibetan lower crust to raise the plateau uniformly in a manner similar to a piston in a hydraulic jack. This model requires a ductile lower crust in southern Tibet. However, *Copley et al.* [2011] investigated the shear stress on the Tibetan Plateau combining fault types and locations and proposed a new model that the Indian crust retains its strength as it underthrusts the Plateau, and couples with the upper crust of southern Tibet. If the lower crust of southern Tibet is ductile, there won't be a coupled deformation. Therefore, whether there is partial melting across the entire plateau, regionally distributed or no melting at all is important question for the injection model.

Usually, a high  $V_p/V_s$  ratio means low  $S$  velocity, which may correspond to partial melting. In contrast, a low  $V_p/V_s$  ratio means no partial melting. Fig. 3.6 shows the  $V_p/V_s$  results from the central Qiangtang terrane to northern Indian plate. The  $V_p/V_s$  value varies from place to place. The most distinct feature is that the northern Indian plate's  $V_p/V_s$  values are consistently below the average  $V_p/V_s$

value. Separated by the YZS, the Lhasa terrane and southern Qiangtang terrane have relatively high Vp/Vs ratios. This means no partial melting in the northern Indian plate, but partial melting is possible north of the YZS. However, the Vp/Vs values of the stations from HiClimb, INDEPTH, western part of Namche-Barwa array are not uniform. Thus the partial melting in Tibetan Plateau is not widely spread, and is only limited to certain region.

Based on the above observations, I suggest that the injection model is not favored, because of lack of widely spread partial molten middle or lower crust in southern Tibet.

### 3.5 Conclusions

By analyzing CCP images of all the four arrays, I found that the Moho in southern Tibet dips towards the north, and has no discontinuity nor offset beneath the MBT. These results suggest that continental lithosphere indeed can subduct during continent-continent collision. It does not support the horizontal shortening model of the India lithosphere. The front of the subducting Indian mantle lithosphere is near the YZS, but is not aligned with its surface trace in the Himalayas. The H- $\kappa$  results show that the Vp/Vs values are consistently low in Indian plate, but relatively high in the Tibetan Plateau. This result means that there is no partial melting or low velocity layer in the Himalayas. However, the Vp/Vs ratios in the southern and central Tibetan Plateau suggest localized partial melting.

## Chapter 4: Evidence of Coupled Deformation of Tibetan Crust Underneath the Northern Yadong-Gulu Rift

### 4.1 Introduction

The Tibetan Plateau, the Earth's highest and largest plateau, was generated by the collision between the Indian and Asian plates. Most of the large scale surface structures on the plateau, such as the Main Central Thrust, the Yarlung-Zangbo Suture, the Bangong-Nujiang Suture, and the Kunlun fault are east-west oriented. These east-west geological structures are related to the north-south directed collision. North-south trending normal faults and rift systems are another distinct surface feature in Tibet (Fig. 4.1). The rift systems are dominant tectonics in recent period. They were discovered based on early Landsat images and field observations [Molnar and Tapponnier, 1978; Armijo *et al.*, 1986] and have several interesting features, such as being widely-distributed and uniformly-spaced. Many different methods have applied to investigate the structure underneath these rifts [Kind *et al.*, 1996; Cogan *et al.*, 1998; Yin, 2000; Kapp *et al.*, 2005], and results have contributed to understanding continental rifting and deformation.

Even though the rift systems in Tibet are directly related to the east-west continental extension due to the north-south collision, the mechanics of the continental crust deformation are still debated. Two contrasting models have been proposed to explain crustal deformation (Fig. 4.2). The first model is decoupled deformation between the upper crust and lower crust [Burchfiel *et al.*, 1989; Bird, 1991; Masek *et al.*, 1994; Royden, 1996]. According to this model, the normal faults and rifts exist only in the upper crust, and there is no narrow deformation zone underneath. Several seismic studies on the rift zones in southern Tibet seemed to support the decoupled crustal deformation model. Kind *et al.* [1996] analyzed the INDEPTH-II surface wave dispersion data and receiver function data from stations

in the Yadong-Gulu rift and found a partially molten crustal layer in southern Tibet. This low velocity zone or ductile mid-crust has been seen by others using different methods [Brown *et al.*, 1996; Makovsky *et al.*, 1996; Alsdorf *et al.*, 1998; Li *et al.*, 2003]. Based on the proposed weak, mid-crustal partial melt layer, Nelson *et al.* [1996] suggested that the upper crust of the Tibetan Plateau is decoupled from the lower crust and mantle lithosphere below. Cogan *et al.* [1998] utilized refraction and common mid-point data along the Yadong-Gulu rift and suggested that the middle crust flowed like a fluid.

In the other model, the upper crust is coupled with the lower crust. The whole

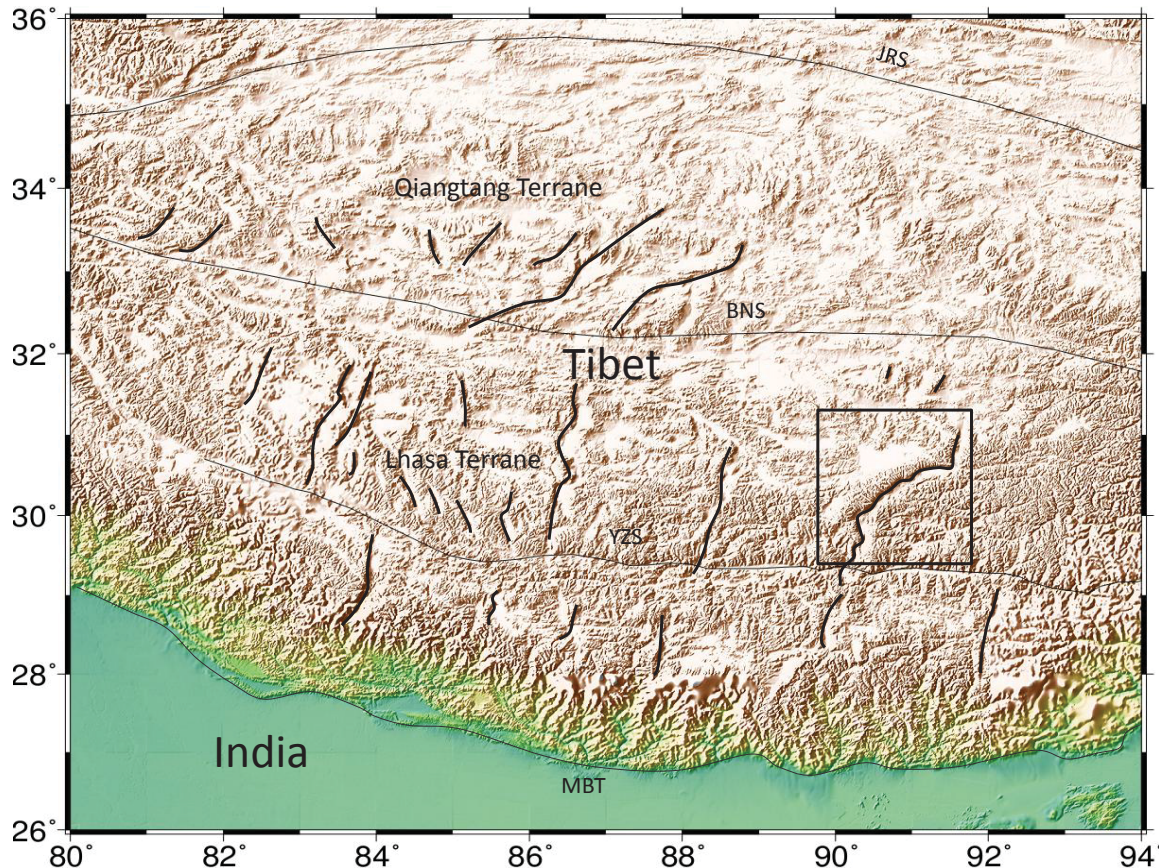


Figure 4.1: Map of the Tibetan Plateau and India. The northern part of the Yadong-Gulu rift beyond YZS is the study area shown within a black square. MBT: the Main Boundary Thrust; YZS: the Yarlung-Zangbo suture; BNS: the Bangong-Nujiang suture; JRS: the Jinsha River suture.

crust deformed in a plate-like behavior and has rift zones penetrating through the entire crust [Tapponnier *et al.*, 1982; Yin, 2000; Copley *et al.*, 2011]. Tapponnier *et al.* [1982] suggested that continental lithosphere behaves as rigid blocks, which have narrow deformation zone across the entire lithosphere. Yin [2000] systematically analyzed the Tibetan rift spacing based on numerical modeling and suggested that the mantle lithosphere of the Tibetan plateau must have been involved in east-west extension. Kapp *et al.* [2005] applied geochemical analyses and surface observation to the exhumed mid-crust exposures of Nyainqntanglha(NQTL) Shan, in the northern part of the Yadong-Gulu rift. The thermochronologic studies of footwall K-feldspars indicated little perturbation of the background thermal structure, which, combined with an undeformed footwall and

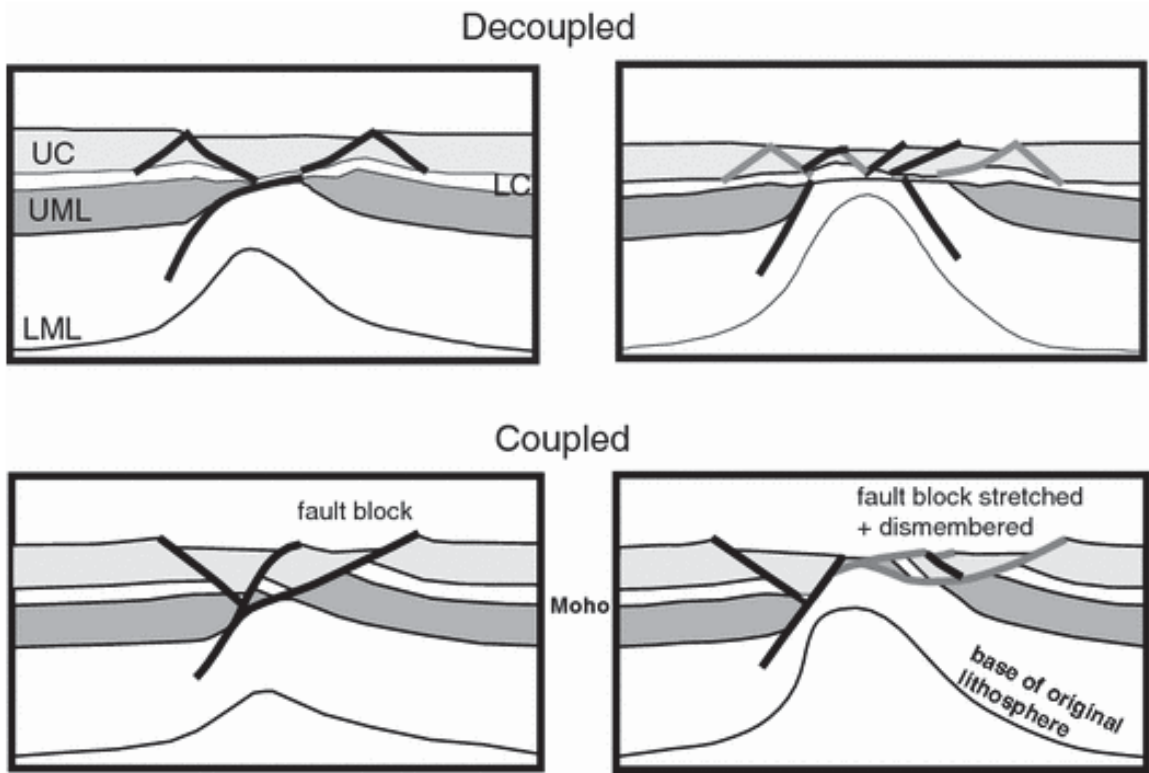


Figure 4.2: Summary of the effects of lower crustal decoupling/coupling on the symmetry of extension. UC upper crust, LC lower crust, UML upper mantle lithosphere, LML lower mantle lithosphere [Reston and Perez-Gussinye, 2007].

the lack of migmatites exposed in the NQTL, indicated that the partial melt zone does not exist or at least in the youngest magmatic episode of this region. *Copley et al.* [2011] investigated the shear stress on the Tibetan Plateau combining faults types and location, and suggested that the Indian crust retains its strength as it underthrusts the Plateau, and couples with the upper crust of southern Tibet.

To examine these two models, I trace the surface deformation near the rifts down to the Moho and investigate whether structural anomalies exist in the lower crust. If localized anomalies indeed exist, the upper crust of Tibet is coupled with the lower crust, and the whole crustal deformation penetrates through the entire crust. Otherwise, if there are smooth or little crustal variations inside the rift zone, that means the upper crust and lower crust are decoupled.

Among these rifts on the Tibetan Plateau, the Yadong-Gulu rift, which is the largest rift, crosses the Yarlung-Zangbo Suture (YZS) and reaches the middle of the Lhasa terrane. In this chapter, the velocity structures of the northern part of this rift beyond the YZS (the black square in Fig. 4.1) are obtained by applying several seismic methods. Over the last two decades, several seismic recording experiments have been carried out in Tibet, such as the INDEPTH project [*Nelson et al.*, 1996; *Zhao et al.*, 2001; *Kind et al.*, 2002] and some permanent stations were deployed, such as the Lhasa station [*Li et al.*, 2011]. I collected seismic data from these stations and applied receiver function techniques [*Zhu and Kanamori*, 2000; *Zhu*, 2000] to stations inside and outside of the Yadong-Gulu rift zone, and also performed a joint-inversion technique with the surface wave dispersion data to investigate the velocity structure beneath the rift and surrounding area. I then compared the results inside and outside the rift to address the question of which model works for deformation of continental lithosphere.

## 4.2 Data and Methods

### 4.2.1 Data processing and receiver functions

Teleseismic  $P$ -wave data from the 1994-1999 INDEPTH II & III arrays and the 1991-1992 LHSA station were collected and processed. Fig. 4.3 shows that 17 stations are distributed near the northern Yadong-Gulu rift (the black square in Fig. 4.1). I applied a 0.05-2.0 Hz band-pass filter to all the seismograms. All the events have magnitudes larger than 5. After visual inspection, more than 1128 teleseismic events with clear  $P$ -wave signals were used to compute receiver functions.

### 4.2.2 H- $\kappa$ determination

After inspecting all receiver functions of each station and discarding stations with noisy waveforms, I retain 9 stations to go through further process (red circles in Fig. 4.3). The first step is computing the  $\kappa$  value using the H- $\kappa$  stacking technique. The  $\kappa$  value is incorporated into each station's velocity model, which is utilized by the CCP stacking technique. The scanning area is  $H$  from 50 to 90 km and  $\kappa$  from 1.5 to 2.0. The LHSA, ST01, ST05 stations have better stacking results than other stations, because these stations have sufficient number of receiver functions. They all have strong Moho  $Ps$  phase as well as the  $PPPs$  and  $PsPs$  multiple phases. An example of the H- $\kappa$  stacking result of ST01 station is shown in Fig. 4.4 and Fig. 4.5. Other nearby stations without clear matching of all three multiple phases, share the  $Vp/Vs$  ratios with the determined stations. In the rift, neither station BB05 nor BB08 has matched multiples. Based on the joint-inversion results (which are discussed later), a better H- $\kappa$  stacking result for station BB08 is obtained by resetting the scanning area to 40 to 65 km by 1.5 to 2.0. Thus the two rift stations share the same  $Vp/Vs$  ratio determined for BB08.

#### 4.2.3 CCP imaging

To image the detail crustal structure across the study area, a CCP stacking image was generated based on the receiver functions and  $\kappa$  values from the 9 stations along the profile shown in Fig. 4.3. The 1-D velocity model of the Tibetan Plateau, which is modified by Zhu (2003), was used to transfer the receiver functions from the time-domain to the depth-domain. The  $V_p/V_s$  ratios of the original model are substituted for the  $\kappa$  values determined by the H- $\kappa$  stacking technique. The

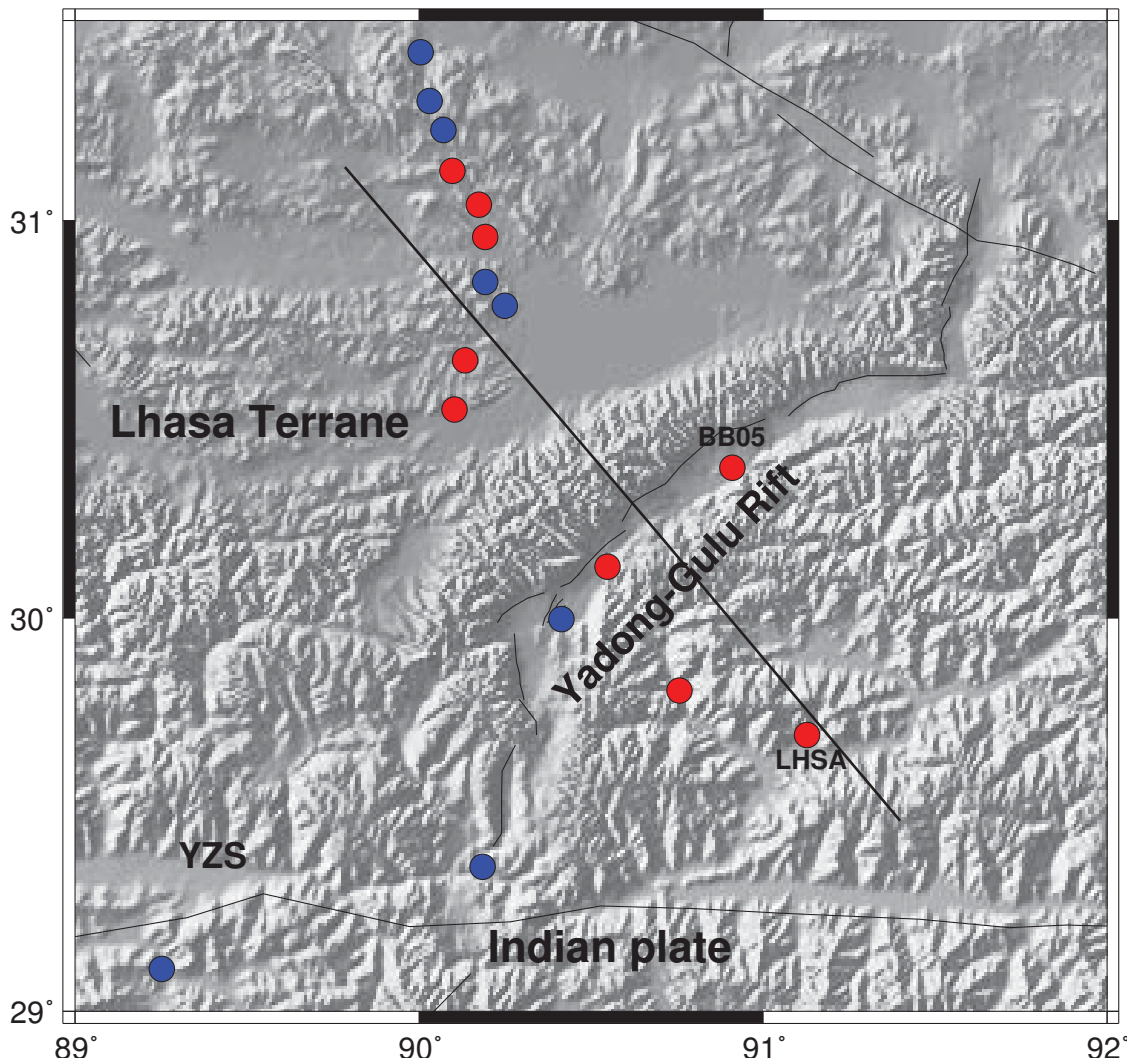


Figure 4.3: All stations are represented by circles. Receiver functions from stations represented by the red circles are utilized to do H- $\kappa$  stacking and CCP stacking. The black line orientated northwest-southeast is the location of the CCP profile.

width of the stacking profile is set to 300 km in order to utilize all the RFs computed from teleseismic  $P$  waves recorded by the stations. The stacking bin size is 1 km wide by 0.5 km high and stacking result of each bin is smoothed with the results of neighboring bins. Although the station intervals are large causing less ray paths in the shallow crust, the structures in the deep crust are well imaged. The Fig. 4.6 shows the CCP stacking result. In this figure, to the southeast of the rift, the Moho is 70 to 80 km deep. Beneath the rift zone, there are three interfaces, which, from the top to bottom, are at 10 to 15 km, 45 to 50 km and 70 km. To the northwest, a relatively flat Moho is at 65 km depth.

#### 4.2.4 1-D velocity model from joint-inversion

To further determine the velocity structures beneath the rift, a joint-inversion technique [*Julia et al.*, 2000] was applied to station BB05 inside the rift zone and station LHSA outside the rift. The surface wave dispersion data were obtained by *Xu and Song* [2010]. A modified IASP91 model is utilized as the starting model for station BB05. A low velocity sedimentary layer [*Cogan et al.*, 1998] and a 15 km deep interface [*Brown et al.*, 1996; *Makovskiy et al.*, 1996] are added to the IASP91 model. I performed the joint inversion with a maximum surface wave period of 70 s and with a 20 s receiver function starting 5 s before the first  $P$  arrival. The weight ratio between RFs and surface wave dispersions is 4:1. The inverted velocity model reaches 150 km maximum depth. In Fig. 4.7, the joint inversion result for station LHSA shows only one large velocity jump at 70 to 80 km depth. Within the rift zone, because of the complicated velocity structure in the upper crust, I put a single velocity layer between the sedimentary layer and the 15 km-deep interface. This velocity model, which is shown in Fig. 4.7, generates synthetic receiver functions and dispersions that match the data well. In this figure, station BB05 shows that the 12 to 15 km and 50 to 55 km deep interfaces are very sharp compared with the

gradually increasing velocity layer at 70 km depth. The joint-inversion results are consistent with the CCP stacking results for the interface depths.

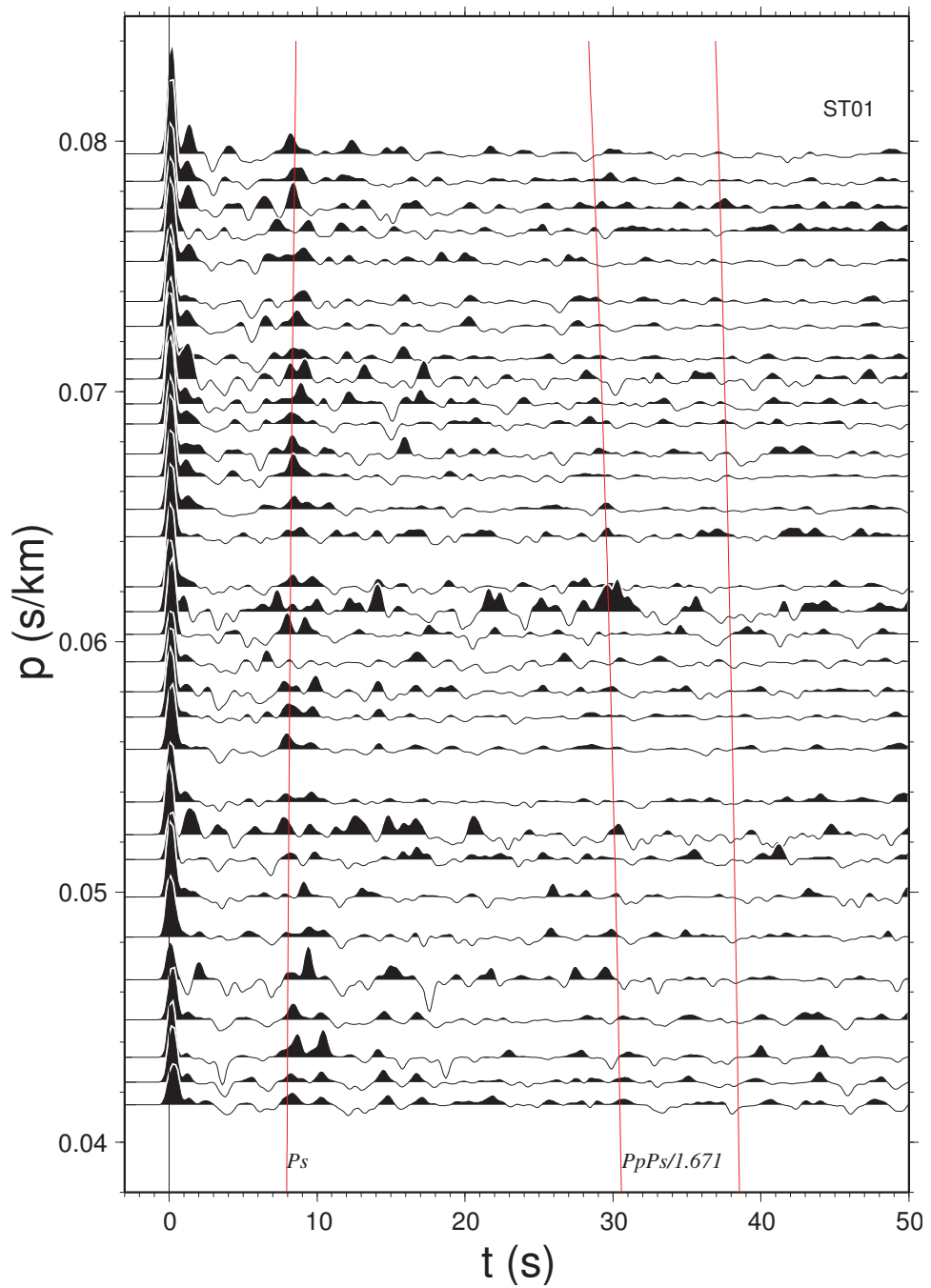


Figure 4.4: Radial receiver function as a functions of ray parameter  $p$  for the 1-D Tibetan Plateau Velocity Model [Zhu, 2003]. the Moho converted phase  $Ps$  and the multiples  $PpPs$ ,  $PpSs$  and  $PsPs$  are labeled.

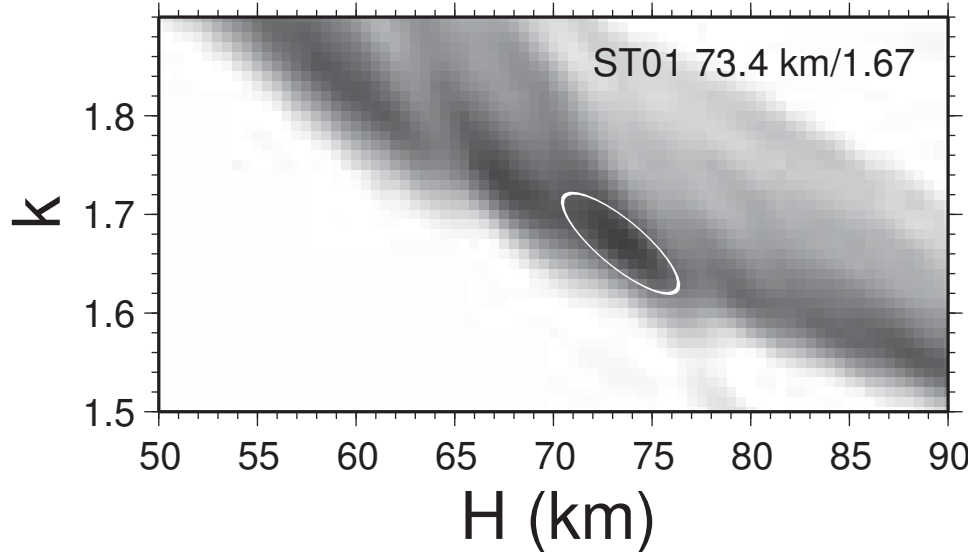


Figure 4.5: The  $s(H, \kappa)$  from stacking the receiver functions in Fig. 2.2. It reaches the maximum (solid area) when the correct crustal thickness and  $V_p/V_s$  ratio are used in the stacking.

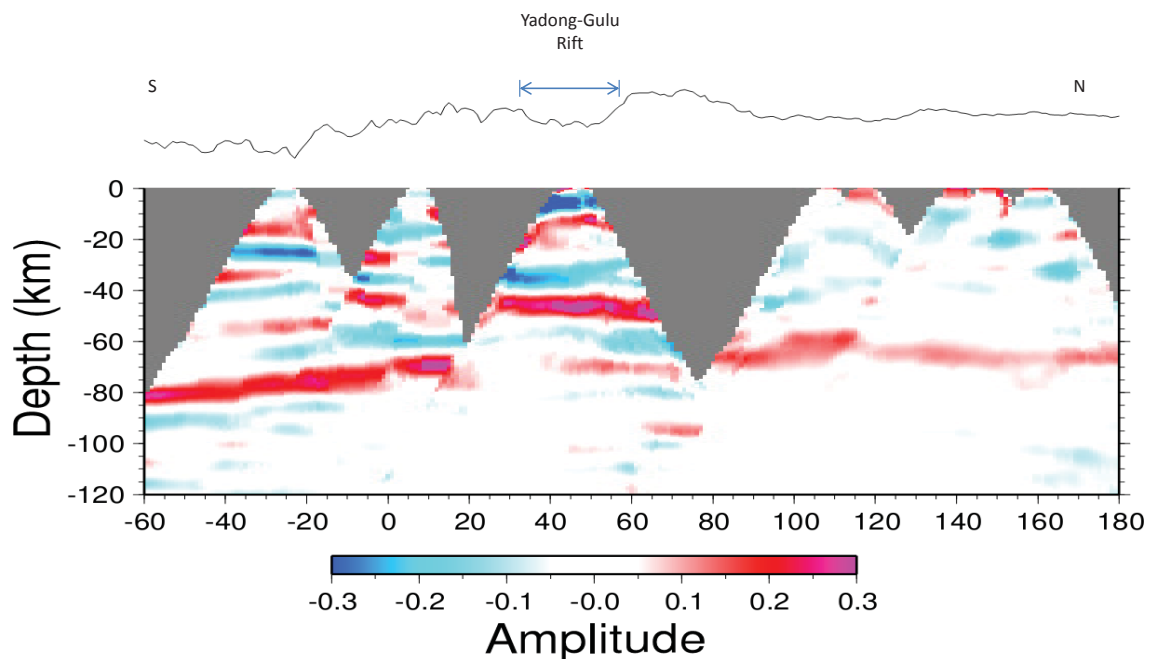


Figure 4.6: The upper figure is the CCP image from profile AB in Fig. 4.3. The red color and blue color represent top to bottom velocity increase or decrease respectively. The gray shape means no data coverage.

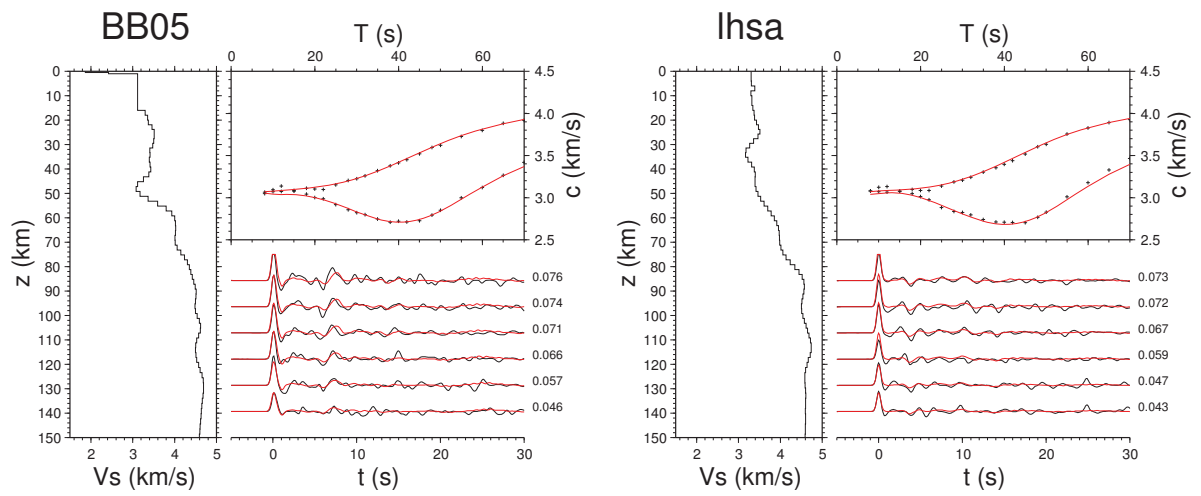


Figure 4.7: The left cartoon is the joint-inversion result for station BB05. The right cartoon is the result of station Lhsa. For each cartoon, the left box is 1-D S-wave velocity profile (in black color). The right top figure is surface wave dispersion data. Black dots are the real data. Red line is the joint-inversion result. Receiver functions and synthetic data are shown in the bottom right. Red traces are synthetic receiver functions.

## 4.3 Discussion

### 4.3.1 Structure inside the northern Yadong-Gulu Rift

In the rift, a low velocity sedimentary layer (see Fig. 4.6) appears in the top 2 km. *Cogan et al.* [1998] estimated the shallow structure of the northern Yadong-Gulu rift by analyzing common midpoint reflection data and found the sediment is less than 1.5 km thick. Although I used different techniques and data, I obtained similar results with them. The common midpoint method generates high-resolution images within 10 km depth range. However, for deeper structure, the receiver function techniques are widely used.

Although the data coverage is not sufficient to review shallow structures along the entire profile, the distinct 12 to 15 km-deep interface within the rift zone is shown in both the CCP image and the joint-inversion results. *Brown et al.* [1996] analyzed INDEPTH I and INDEPTH II reflection data along the Yadong-Gulu rift and detected a strong subhorizontal reflection at 15-18 km depth. An approximately 15 km deep reflector was determined by *Makovskiy et al.* [1996] using wide-angle reflection data. In addition, *Kind et al.* [1996] utilized receiver function methods and joint-inversion methods with Rayleigh wave dispersion data and found a large velocity contrast at 20 km depth north of YZS. Basically, our results agree with these observations of a 15 km deep reflector in the upper crust. However, our receiver function and joint-inversion results (BB05 in Fig. 4.7) show no low velocity layer right beneath the 15 km-deep interface as found by *Kind et al.* [1996], *Brown et al.* [1996], *Makovskiy et al.* [1996], *Alsdorf et al.* [1998] and *Li et al.* [2003]. In the CCP image (Fig. 4.6), the 15 km-deep interface has a strong positive amplitude, which means velocity increases with depth. The shear wave velocity profile shows an obvious velocity jump at this depth (Fig. 4.7). [*Kapp et al.*, 2005] suggested that the rift is in its early stage of magmatism and there is no partial melting in the

upper crust yet. Therefore, the 15 km-deep interface is not the upper boundary of the proposed weak, mid-crustal partial melt layer by *Nelson et al.* [1996].

A lower crustal interface at 50 km depth is another interesting feature in the rift zone. This interface can be seen in the CCP image and joint-inversion results with the largest amplitude and a positive velocity jump. Compared with the 70 km weak interface in the CCP image (Fig. 4.6), the 50 km one is much stronger and sharper. The Moho, which separates basaltic crust and peridotite mantle, usually has the largest velocity contrast in the crust. However, the shear wave velocity profile beneath BB05 and BB08 show that the shear wave velocity beneath the 50 km interface is a little less than 4 km/s. This value is higher than the Tibetan crust velocity of 3.5 km/s, but lower than the mantle velocity of 4.4 km/s [*Chen and Molnar, 1981*]. *Stratford and Stern* [2006] estimated the crustal structure beneath the Central Volcanic Region in New Zealand by wide-angle reflection and refraction methods. They found a similar structure with two interfaces in the lower crust beneath the rift zone. Between the interfaces, the  $P$  wave velocity is 6.8-7.3 km/s, which is between the classic crust and mantle velocities. They interpreted the layer in between as new igneous crust due to the high heat flow and volcanic activity. Nevertheless, it's difficult to tell which interface is the Moho without other data. A similar situation applies to our research area. In spite of the uncertainty in Moho depth, it is clear that the velocity structure beneath the northern Yadong-Gulu rift is very different from the outside region, especially in the lower crust level.

#### 4.3.2 Structure outside the northern Yadong-Gulu Rift

Outside the Yadong-Gulu rift zone, a simple crustal structure without multiple interfaces or low velocity zone is shown in the velocity model and CCP image (Fig. 4.6). To the northwest of the rift, there is only one interface at about 70 km. I interpret it as the Moho, which is comparable with the previous results by *Ross*

*et al.* [2004]. To the southeast of the Yadong-Gulu rift, the Moho is seen clearly at close to 80 km depth in both the joint-inversion results for station LHSA (Fig. 4.7) and the CCP image (Fig. 4.6). In this region, a 70-80 km Moho was also observed earlier using different seismic techniques by *Zhao et al.* [1993], *Kind et al.* [1996] and others. Although some positive energy in the crust is seen in the CCP image (Fig. 4.6), it is likely to be caused by noise. In Fig. 4.7, a relatively smooth velocity profile above the Moho is shown in the joint-inversion result of LHSA station. This indicates that the anomalous structure beneath the northern Yadong-Gulu rift does not extend outside of the rift zone.

#### 4.4 Conclusion

All the results from receiver functions' H- $\kappa$  stacking, CCP stacking and joint-inversion with surface wave dispersion data suggest a narrow zone beneath the Yadong-Gulu rift where the crustal structure is different from outside the rift zone. This indicates that the east-west extension deformation of Tibetan Plateau is localized in several vertical narrow rift zones through the entire crust. The Yadong-Gulu rift is the largest rift on Tibet. It is representative of most of rift systems on the Tibetan Plateau. Thus based on the localized deformation observed by receiver functions techniques, the plate-like behavior of a rigid continental lithosphere deformation model is favored.

## Chapter 5: Crustal Structure of the Central Tien Shan Orogenic Belts from Receiver Function Studies

### 5.1 Introduction

The Tien Shan in central Asia is the largest and most active intercontinental orogen in the world. This orogen extends in a east-west direction for about 2500 km, and its highest peak has an elevation above 7000 m. The Tien Shan is located nearly 2000 km north of the Indian and Asian collision zone, separated from the Tibetan Plateau by the Tarim Basin. The Kazakh Shield is to the north of this orogen (Fig. 5.1).

The Tien Shan is similar to the Tibetan Plateau. Both regions are very active recently (since 8 Ma). *Tapponnier and Molnar* [1979] proposed that the tectonic activity of Tien Shan is attributed to the Indian-Asian collision, probably because the Indian plate is moving northwards and pushing the Tibetan Plateau towards the Tarim Basin. The relatively rigid Tarim block [*Vilotte et al.*, 1984; *Neil and Houseman*, 1997], undergoing little internal deformation, transfers the stress to the Tien Shan to form an intercontinental collision zone. The plates involved in the colliding process are both continental lithosphere. Thus, besides the Tibetan Plateau, the Tien Shan is also a prime candidate for studying uplift and deformation during convergence between continental lithospheres.

The ancestral Tien Shan was formed during mountain building in the Paleozoic, which was a result of collision events of many continental blocks, island arcs, and accretion prisms [*Burtman*, 1975]. From the Mesozoic to the early Cenozoic, the ancestral Tien Shan experienced erosion and was turned into a peneplain [*Avouac and Tapponnier*, 1993; *Metivier and Gaudemer*, 1997]. The intracontinental orogenesis resumed in the Oligocene and is still active presently [*Sobel and Dumitru*, 1997; *Chen et al.*, 1999; *Molnar and Ghose*, 2000], presumably as a

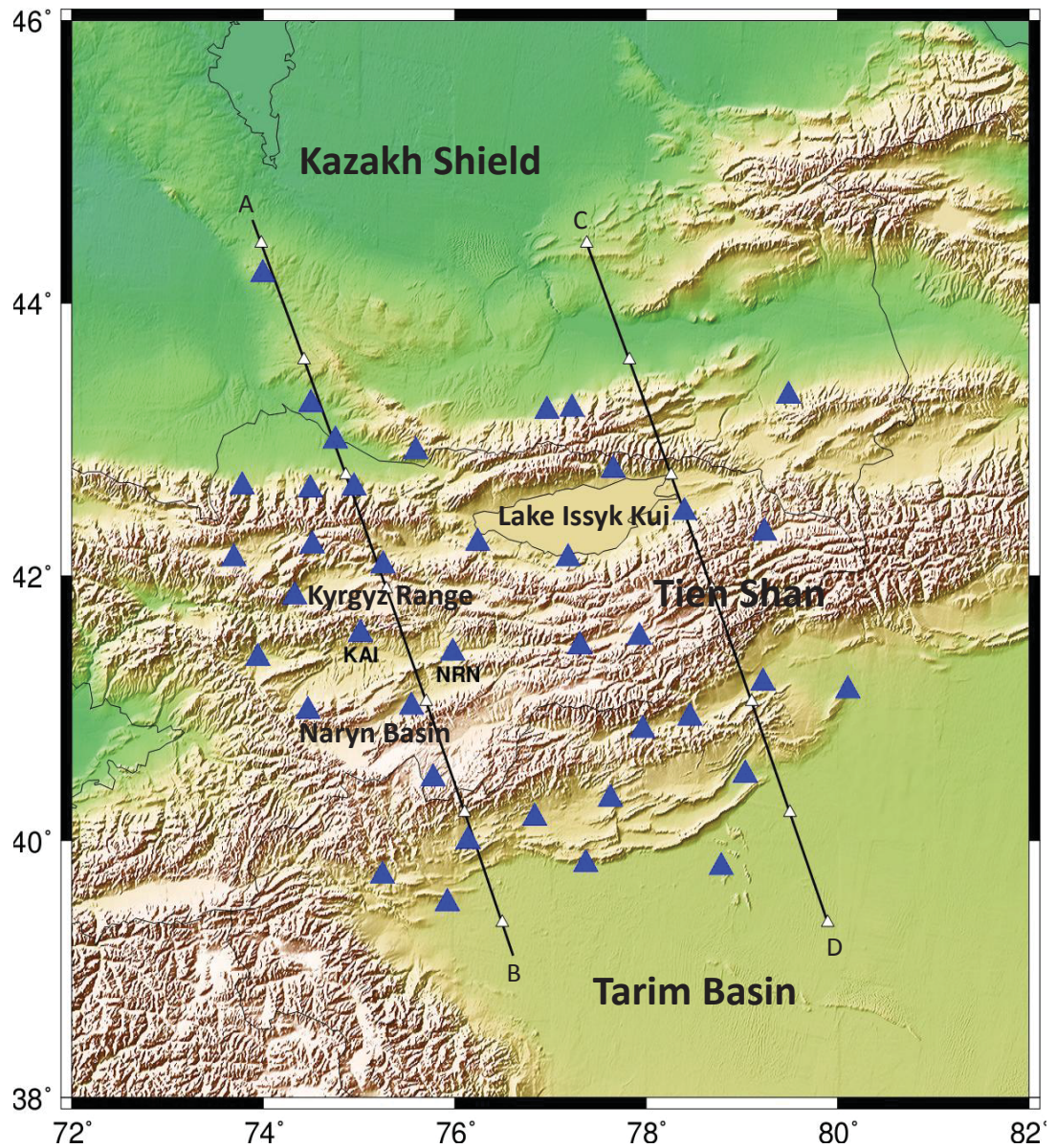


Figure 5.1: Map of the research area. The blue triangles are the stations from NANGA KNET, GSN, GEOSCOPE and GHENGIS networks. The KAI and NRN stations are in the Naryn Basin and are utilized to perform the surface-wave and receiver function joint-inversion. Two profiles AB and CD oriented from northwest to southeast are used to image the crustal structure.

consequence of Indian-Asian collision [Tapponnier and Molnar, 1979].

Although the Indian-Asian collision might be the cause of the revival of tectonic

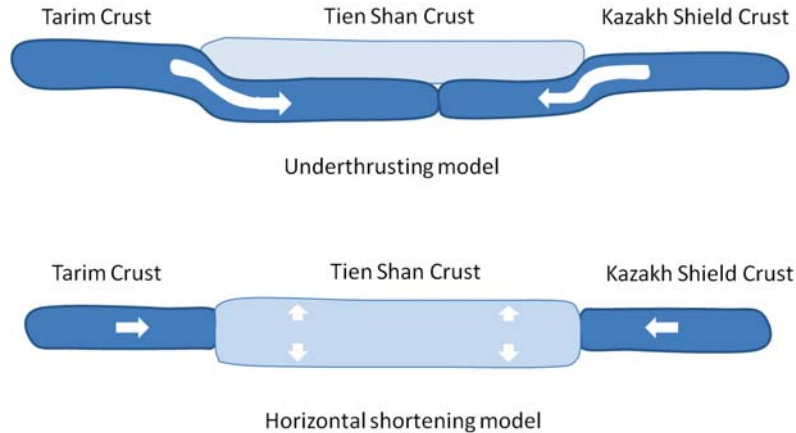


Figure 5.2: The top figure is a sketch of underthrusting model. The bottom figure is a sketch of horizontal shortening model.

activity of the Tien Shan, the details of the mountain building mechanism are still controversial. *Fleitout and Froidevaux* [1982] proposed a crustal shortening model to explain the uplift of the Tien Shan, which was associated with lithosphere thickening. Due to the indentation of India to Eurasia, the dominate deformation style of this range is north-south compression. Geological surveys, earthquake focal mechanisms and GPS observations show that the Tien Shan is undergoing significant north-south shortening at a rate of 20 mm/yr [*Abdrakhmatov et al.*, 1996; *Thompson et al.*, 2002; *Xu et al.*, 2008; *Yang et al.*, 2008]. Some other researchers suggested that the Orogenesis of the Tien Shan was caused by the underthrusting of the Tarim Basin from the south and the Kazakh Shield from the north, based on seismic tomographic imaging [*Roecker et al.*, 1993; *Lei and Zhao*, 2007; *Lei*, 2011], focal mechanisms [*Ni*, 1978; *Nelson et al.*, 1987] and receiver function analysis [*Chen et al.*, 1997]. The Fig. 5.2 shows a sketch of these two models.

Knowing the mechanism of the Tien Shan mountain building will help us to understand plate tectonics for continental lithosphere. The Moho, as the most prominent discontinuity which separates the crust from the mantle, can provide important information regarding lithospheric deformation. If the Tarim Basin or

Kazakh shield are underthrusting beneath the Tien Shan, a dipping Moho should be observed near the block boundaries, or there might be two Mohos beneath the Tien Shan. (the Tien Shan's Moho on top of the underthrusting Tarim Basin or Kazakh Shield Mohos) If the lithosphere shortening or mantle upwelling play the dominant role in the Tien Shan uplift, sharp Moho depth changes or vertical Moho offsets might be found near the northern or southern Tien Shan edges.

Many RF and tomography studies have been conducted in the Tien Shan region [Roecker *et al.*, 1993; Kosarev *et al.*, 1993; Chen *et al.*, 1997; Bump and Sheehan, 1998; Xu *et al.*, 2002; Vinnik *et al.*, 2004; Kumar *et al.*, 2005; Lei and Zhao, 2007]. The crust beneath the Tien Shan is 10 km thicker than beneath the Kazakh Shield [Chen *et al.*, 1994; Bump and Sheehan, 1998; Vinnik *et al.*, 2004]. Cold lithosphere materials near 410 km depth beneath the Tien Shan are detected by  $P$  receiver functions [Chen *et al.*, 1997], which is consistent with tomography imaging using a similar data set in this region, suggesting a detached piece of the subducting Tarim lithosphere between 200 and 400 km depth [Pavlis *et al.*, 2003]. Tian *et al.* [2010] applied a teleseismic  $P$  wave receiver function method and found that the 410 discontinuity becomes shallower while the 660 discontinuity becomes deeper beneath the south and east of Lake Issyk-Kul, possibly caused by thickened lithosphere dropping down to the bottom of the mantle transition zone. In addition, some researchers observed low velocity anomalies beneath the Tien Shan at 50 km depths, which were also revealed downward beneath the Tarim Basin and the Kazakh Shield [Roecker *et al.*, 1993; Vinnik *et al.*, 2004; Lei and Zhao, 2007]. They suggested that smallscale convection or small mantle plume are possible causes [Sobel and Arnaud, 2000; Friederich, 2003; Vinnik *et al.*, 2004; Wolfe and Vernon, 1998; Tian *et al.*, 2010; Lei, 2011].

In this study, teleseismic receiver function methods were used to determine crustal structural variation of the central Tien Shan. H- $\kappa$  stacking techniques were

applied to determine crustal thickness and Vp/Vs ratios beneath each station [Zhu and Kanamori, 2000]. For two profiles where station intervals are small, high resolution images of the crust and uppermost mantle will be obtained using the CCP stacking method [Zhu, 2000]. Also I performed joint-inversion of receiver functions with surface wave dispersion to obtain *S*-wave profiles to constrain the crustal structures. The interpretations and implications are discussed based on the results.

## 5.2 Data

Seismic data from 4807 teleseismic earthquakes recorded by 53 stations from 1995 through 2007 are collected and processed. Fig. 5.1 shows the research area and the distribution of all stations. Only the events with magnitudes larger than 5 are utilized and plotted as blue dots in Fig. 5.3. The back-azimuths of the events cover most directions. More events are located to the east than to the west. The stations are from NANGA KNET, GSN, GEOSCOPE and GHENGIS networks, which are deployed in or around the Tien Shan and the Tarim basin. I applied a 0.05-2.0 Hz band-pass filter to all the seismograms. After visual inspection, 25869 RFs are obtained to image the crustal structure.

Fig. 5.4 show typical receiver functions. The receiver functions are plotted in the order of back-azimuth. Similar to Fig. 5.3, the data coverage is very dense from the east and south, but relatively sparse from the north and north-west.

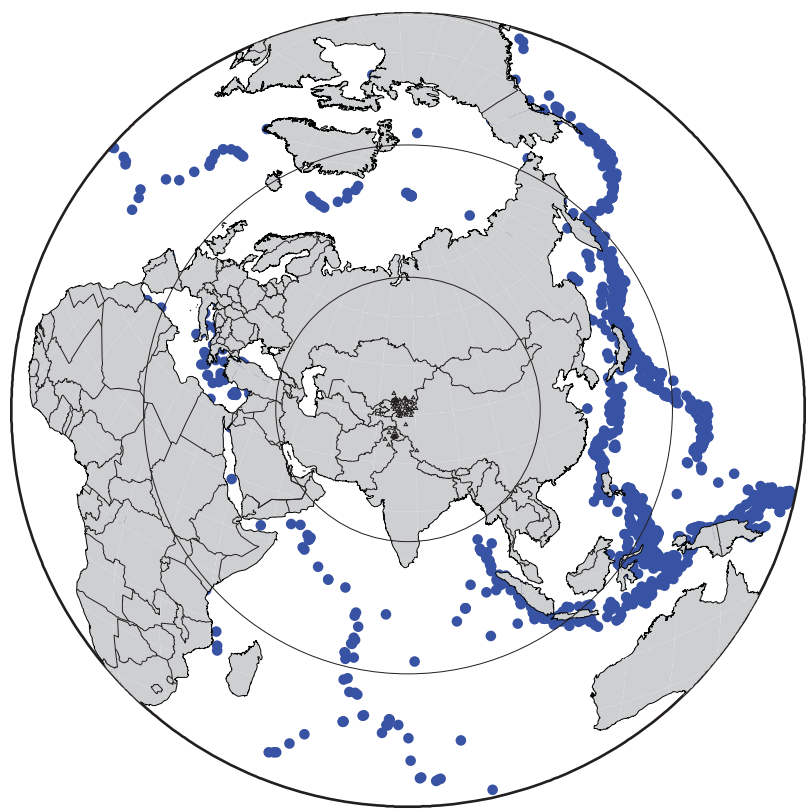


Figure 5.3: Locations of the 53 broadband stations in the research area are shown as black triangles. The blue circles are the selected events recorded by these stations.

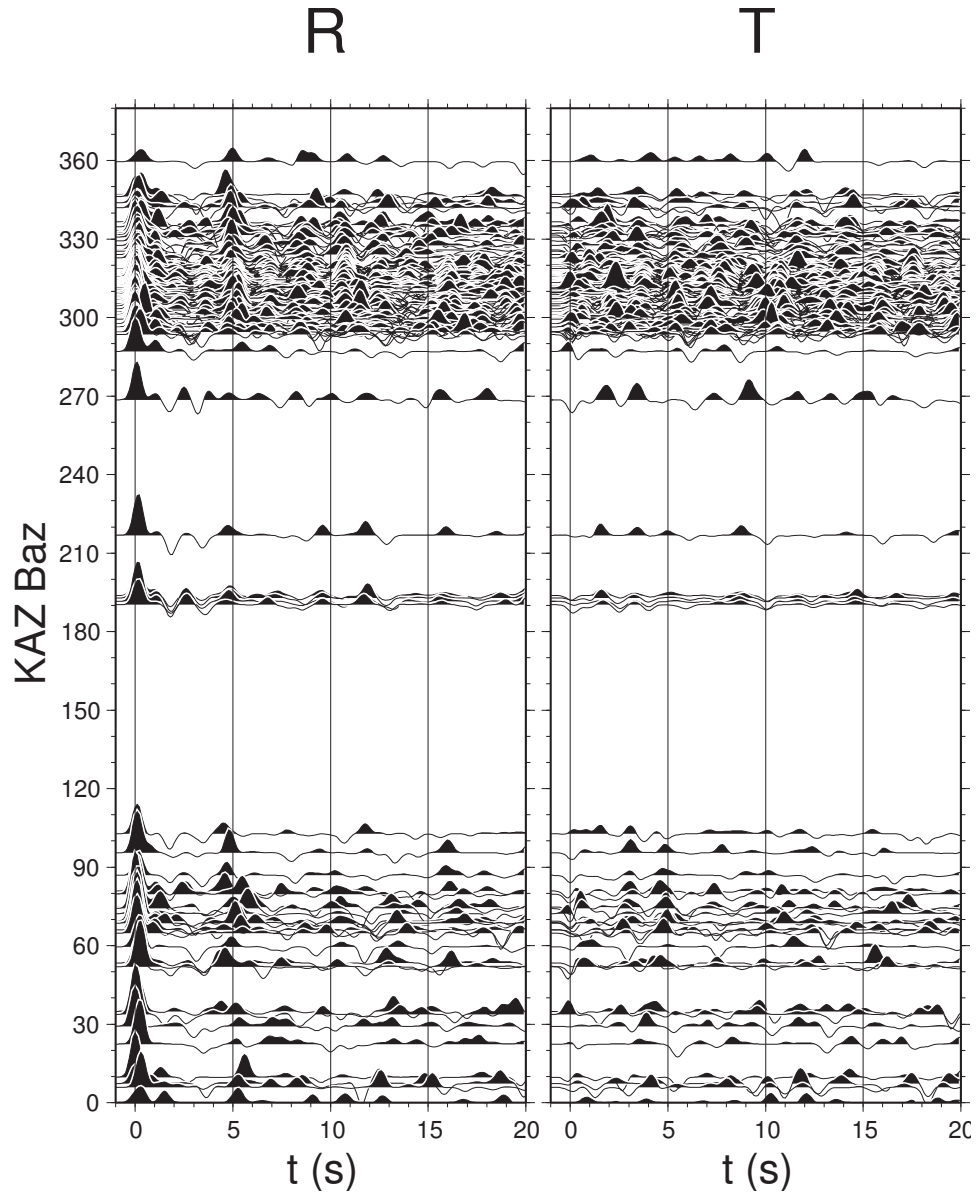


Figure 5.4: Teleseismic  $P$  wave receiver functions plotted in the order of back-azimuth. R and T represent radial and transverse components, respectively.

### 5.3 Results from Receiver functions studies

The crustal structure images are computed by CCP stacking along the profiles shown in Fig. 5.1. These two profiles are both oriented from northwest to southeast, centered at 42° N, 75° E and 42° N, 79° E respectively. The stacking bin size is 1 km along the profile, 100 km perpendicular to the profile, and 0.5 km in depth. The width of the stacking profile is 300 km. Along the western profile (Fig. 5.5), a simple Moho interface is at 45 km depth beneath the Kazakh shield and starts dipping southward at the northern boundary of the Tien Shan. It terminates at 80 km depth beneath the Kyrgyz Range. The CCP image beneath the Tien Shan mountain range is complex. The Moho interface extends from the southern boundary of the Tien Shan at 50 km depth towards the north, to about 60 km depth south of the Naryn Basin. It then becomes shallow to about 40 km depth below the Naryn Basin, and deepens to 50 km beneath the Kyrgyz Range, finally ending at the northern boundary of the Tien Shan. The black crosses represent the crustal thickness determined by the H- $\kappa$  stacking method from individual stations. For the eastern profile (Fig. 5.6), the Moho interface beneath the Tien Shan is relatively simple compared with in the west. Only one sharp interface is present and is at depth between 50 km and 60 km. The Moho becomes shallower approaching the northern and southern boundaries. A southward dipping interface is beneath the northern boundary, and terminates at 80 km depth.

In addition to the receiver function techniques, the joint-inversion technique is applied to obtain the velocity structure beneath the Naryn Basin. The IASP91 model is utilized as the starting model for stations KAI and NRN near the Naryn Basin. I performed a joint inversion of surface wave dispersions and receiver functions. The weight ratio between RFs and surface wave dispersions is 4:1. In Fig. 5.7, the joint inversion result of station KAI shows a gradual velocity increase starting at 40 km depth and continuing to 55 km depth. The theoretical RFs and

dispersions for this velocity model match the data well. The station NRN inversion result shows a 35 km depth sharp interface and a layer with velocity gradually increasing with depth to 50 km depth.

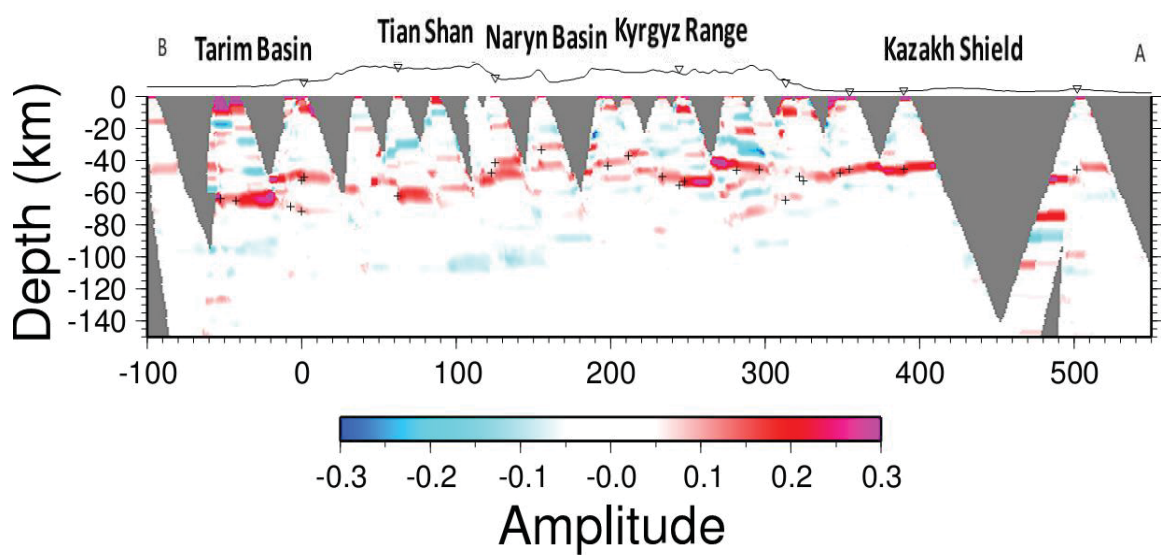


Figure 5.5: The crustal structure imaged by CCP stacking method along the western profile in Fig. 5.1. The black crosses show the crustal thickness from the H- $\kappa$  stacking method.

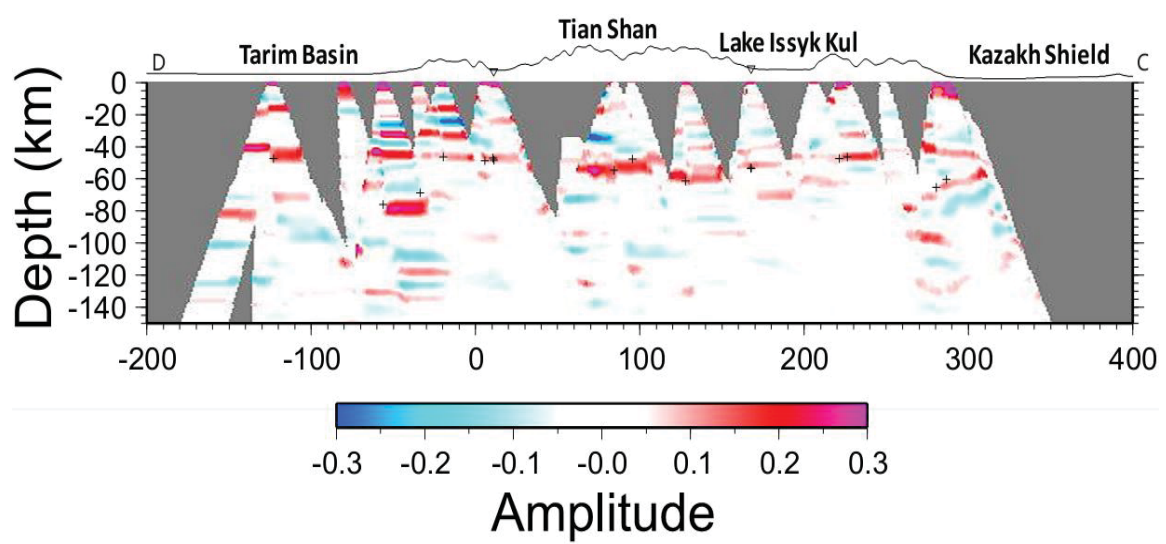


Figure 5.6: The crustal structure imaged by CCP stacking method along the eastern profile in Fig. 5.1.

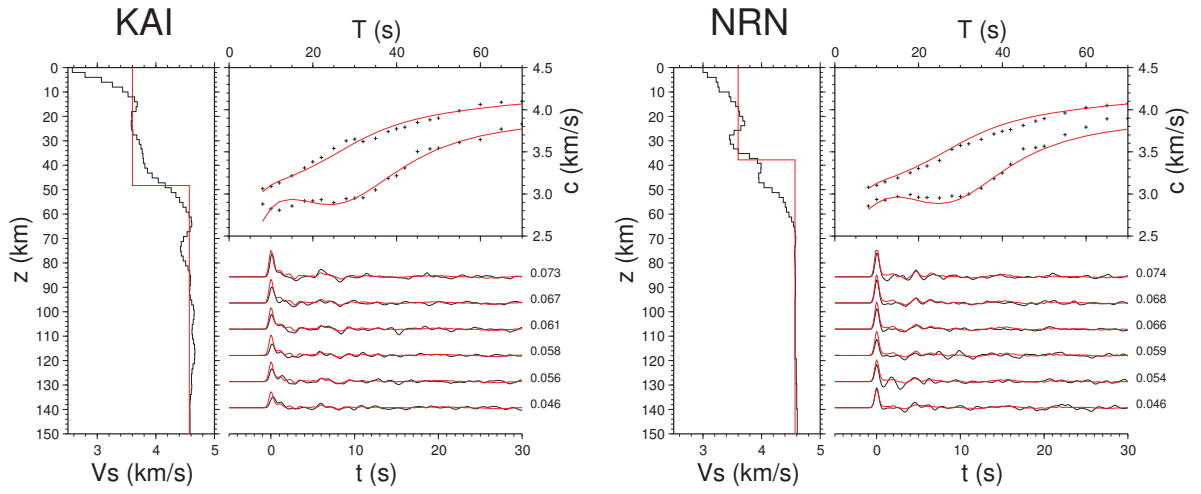


Figure 5.7: The left panel is the joint-inversion result of station KAI. The right panel is the result of station NRN. For each panel, the left box is 1-D S-wave velocity profile (in black color). The right top figure is surface wave dispersions. Black dots are real data, red line is the joint-inversion result. Receiver functions are shown at the bottom (Red traces are synthetic receiver functions).

## 5.4 Discussion

My results show a Moho single interface in southern Tien Shan and the Tarim Basin. The continuous Moho starts from the Tarim Basin at 40 – 45 km depth to 60 – 70 km depth beneath the central Tien Shan. There is no dipping interface beneath the northern edge of the Tarim Basin. *Vinnik et al.* [2004] combined P and S wave receiver functions to obtain tomographic images of the Tien Shan. They observed similar Moho depths in the southern Tien Shan and Tarim Basin, about 60 km and 45 km, respectively. *Nelson et al.* [1987] computed several earthquakes focal mechanisms at the southern edge of the Tien Shan to constrain the fault plane orientation and depth. Some underthrusting faults were indicated by four events, deeper than 20 km depth. According to my RF results, the Moho of the Tarim Basin is over 40 km deep, deeper than those earthquakes. So these events' mechanisms do not imply that the thrusting faults extend to the Moho level. The lack of dipping interfaces beneath the boundary of Tarim and Tien Shan suggests that the horizontal shortening caused by the compressing from the Tarim Basin is likely to be the mechanism of the Tien Shan's uplift.

The northern Tien Shan and Kazakh Shield have relatively complex deep structures (Fig. 5.5 and Fig. 5.6). The Moho beneath the Kazakh Shield is at around 45 km depth, and dips southward beneath the northern edge of the Tien Shan. The dipping Moho reaches nearly 80 km depth at about 80 km south of the boundary. The Tien Shan's Moho is above this dipping interface, at about 55 km depth. Based on previous studies, the crust beneath the Tien Shan is 10 km thicker than that beneath the Kazakh Shield [*Bump and Sheehan*, 1998; *Vinnik et al.*, 2004]. However, they didn't observe the dipping Moho in the region. *Ni* [1978], *Nelson et al.* [1987], *Roecker et al.* [1993] and *Chen et al.* [1997] suggested that the Kazakh Shield lithosphere is underthrusting beneath the Tien Shan, causing the uplift of the orogen. According to my results, only one clear Moho beneath the Tien

Shan is observed, which suggests that the Kazakh Shield and Tarim Basin are not underthrusting underneath the Tien Shan's crust. The dipping Moho beneath the north edge may represent the underthrusting or bending of the Kazakh Shield crust but it stops at the northern edge of the Tien Shan.

A shallow Moho beneath the Naryn Basin is revealed by the CCP stacking and H- $\kappa$  stacking results (Fig. 5.5). Instead of 60 km in surrounding areas, the Moho depth beneath the Naryn Basin is near 50 km. In addition, a gradual velocity increasing layer at around 50 km depth, is shown in the 1-D  $S$ -velocity model from the joint inversion of RFs and surface wave dispersion (Fig. 5.7). Previous researchers found some low velocity, high Poisson's ratio anomalies in the deep crust and upper mantle beneath central Tien Shan, which might represent a upwelling of hot and wet mantle materials [Sobel and Arnaud, 2000; Friederich, 2003; Vinnik *et al.*, 2004; Wolfe and Vernon, 1998; Tian *et al.*, 2010; Lei, 2011]. Thus the shallow Moho beneath the Naryn Basin could be caused by the upwelling of mantle materials.

Fig. 5.8 is an interpretation based on the RFs and surface wave dispersion results shown in Figs. 5.5, 5.6, and 5.7. The uplift of the Tien Shan is caused by horizontal shortening and compression from both directions.

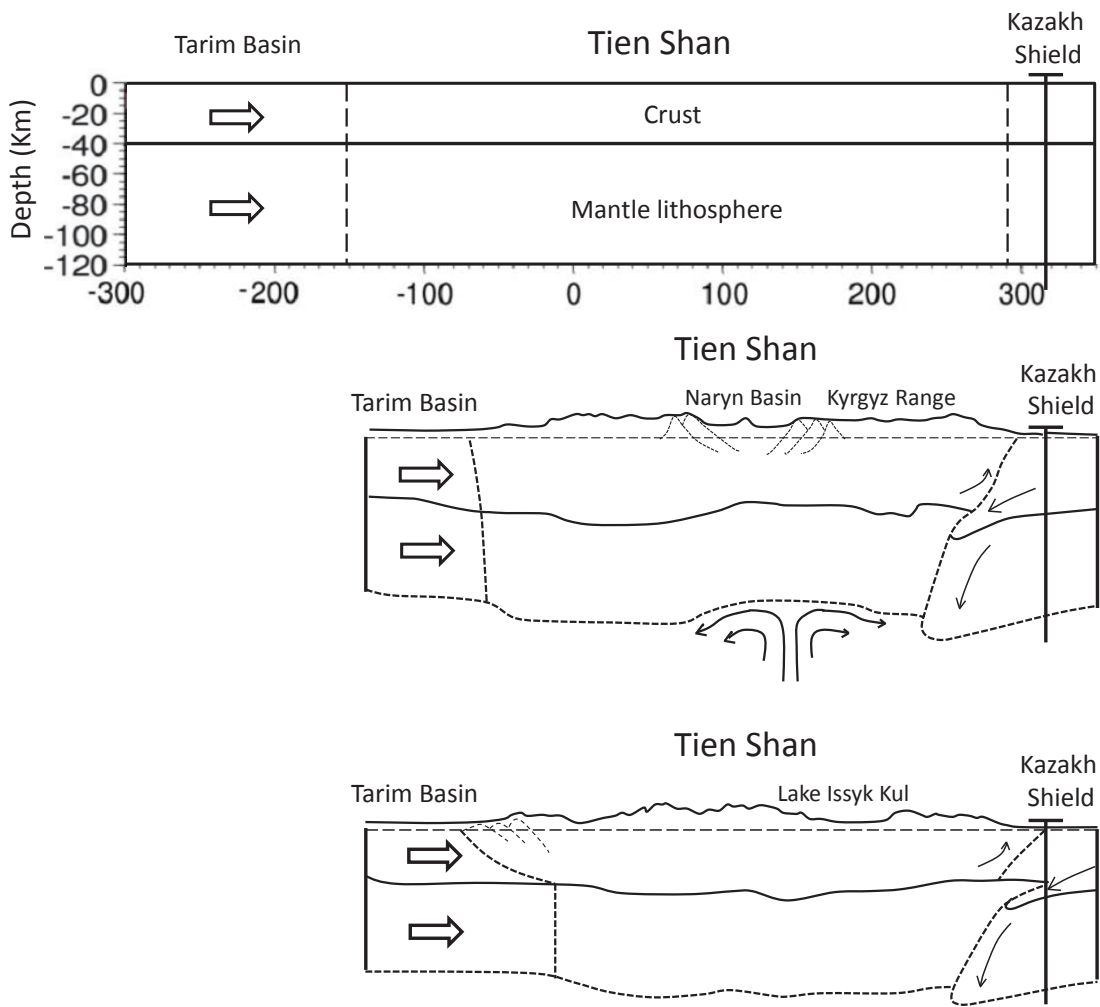


Figure 5.8: The top figure shows the initial configuration before the uplift of the Tien Shan. The Kazakh Shield is fixed and the Tarim basin is moving towards the Tien Shan. The middle figure shows an interpretation of CCP image of profile AB, the bottom shows an interpretation of CCP image of profile CD.

## 5.5 Conclusion

Using receiver function techniques, I investigate the crustal structure of the Tien Shan and its surrounding area. The results suggest that there is not a dipping interface at the edge of the Tarim basin and Tien Shan. Even though there is an interface dipping from the Kazakh Shield to the north, it stops about 80 km south of the northern edge of the Tien Shan. Since no underthrusting Kazakh Shield and Tarim Basin's Moho are imaged underneath the Tien Shan's crust, the resumption of mountain building 20 Ma should be attributed to the horizontal shortening from both sides of the Tien Shan. The shallow Moho beneath the Naryn Basin might be caused by the upwelling of hot mantle materials. However, the resumption of the Tien Shan activity is not necessary related to this mantle upwelling.

## References

- Abdrakhmatov, K. Y., et al., Relatively recent construction of the Tien Shan inferred from GPS measurements of present-day crustal deformation rates, *Nature*, 384, 450–453, 1996.
- Alsdorf, D., L. Brown, K. D. Nelson, Y. Makovsky, S. Klempner, and W. Zhao, Crustal deformation of the Lhasa terrane, Tibet Plateau from project INDEPTH deep seismic reflection profiles, *Tectonics*, 17, 501–519, 1998.
- Armijo, R., P. Tapponnier, J. L. Mercier, and T. Han, Quaternary extension in southern Tibet: Field observation and tectonic implications, *J. Geophys. Res.*, 91, 13,803–13,872, 1986.
- Avouac, J. P., and P. Tapponnier, Kinematic model of active deformation in central Asia, *Geophys. Res. Lett.*, 20, 895–898, 1993.
- Bird, P., Lateral extrusion of lower crust from under high topography in the isostatic limit, *J. Geophys. Res.*, 96, 10,275–10,286, 1991.
- Bird, P., and K. Piper, Plane-stress finite-element models of tectonic flow in southern California, *Phys. Earth Planet. Inter.*, 21, 158–175, 1980.
- Brown, L. D., et al., Bright spots, structure, and magmatism in Southern Tibet from INDEPTH seismic reflection profiling, *Science*, 274, 1688–1690, 1996.
- Bump, H., and A. Sheehan, Crustal thickness variations across the northern Tien Shan from teleseismic receiver functions, *Geophys. Res. Lett.*, 25, 1055–1058, 1998.
- Burchfiel, C. B., Q. Deng, P. Molnar, L. H. Royden, Y. Wang, P. Zhang, and W. Zhang, Intracrustal detachment with zones of continental deformation, *Geology*, 17, 748–752, 1989.
- Burtman, V. S., Structural geology of variscan Tien Shan, USSR, *American Journal of Science*, 275, 157–186, 1975.
- Chen, C., H. Lu, D. Jia, D. Cai, and S. Wu, Closing history of the southern Tian shan oceanic basin, western China: an oblique collisional orogeny, *Tectonophysics*, 302, 23–40, 1999.
- Chen, H., G. Kosarev, and S. Roecker, Shear wave velocity structure at depths 0–410km determined by the teleseismic broadband P-waveforms in northern Pakistan and Kirghizstan, *EOS Trans, AGU*, 75, 464, 1994.
- Chen, W. P., and P. Molnar, Constraints on the seismic wave velocity structure beneath the Tibetan Plateau and their tectonic implications, *J. Geophys. Res.*, 86, 5937–5962, 1981.

- Chen, Y., S. Roecker, and G. Kosarev, Elevation of the 410 km discontinuity beneath the central Tien Shan: Evidence for a detached lithospheric root, *Geophys. Res. Lett.*, 24, 1531–1534, 1997.
- Cogan, M. J., K. D. Nelson, W. S. F. Kidd, C. Wu, and P. I. Team, Shallow structure of the Yadong-Gulu rift, southern Tibet, from refraction analysis of project INDEPTH common midpoint data, *Tectonics*, 17, 46–61, 1998.
- Copley, A., J. P. Avouac, and B. P. Wernicke, Evidence for mechanical coupling and strong Indian lower crust beneath southern Tibet, *Nature*, 472, 79–81, 2011.
- Dewey, J. F., R. M. Shackleton, C. Chang, and Y. Sun, The tectonic evolution of the Tibetan Plateau, *Phil. Trans. R. Soc. Lond.*, 327, 379–413, 1988.
- Dobretsov, G. I., and I. A. Zagruzina, Young basaltoid igneous activity in the eastern Tien Shan, *Trans (Dokl) USSR Acad. Sci., Earth Sci.*, 235, 67–70, 1977.
- England, P., and G. Houseman, Finite strain calculations of continental deformation, 2, comparison with the India-Asia collision zone, *J. Geophys. Res.*, 91, 3664–3676, 1986.
- England, P., and D. P. McKenzie, A thin viscous sheet model for continental deformation, *Geophys. J. R. Astron. Soc.*, 70, 295–321, 1982.
- England, P. C., and G. Houseman, The mechanics of the Tibetan Plateau, *Philosophical Transactions of the Royal Society, London*, 326, 301–319, 1988.
- Fielding, E., B. Isacks, M. Barazangi, and C. Duncan, How flat is Tibet?, *Geology*, 22, 163–167, 1994.
- Fleitout, L., and C. Froidevaux, Tectonics and topography for a lithosphere containing density heterogeneities, *Tectonics*, 1, 21–56, 1982.
- Friederich, W., The S-velocity structure of the East Asian mantle from inversion of shear and surface waveforms, *Geophys. J. Int.*, 153, 88–102, 2003.
- Haines, S. S., S. L. Klemperer, L. Brown, J. Guo, J. Mechie, R. Meissner, A. Ross, and W. Zhao, INDEPTH III seismic data: From surface observations to deep crustal processes in Tibet, *Tectonics*, 22, 1001–1019, 2003.
- Hauck, M. L., K. D. Nelson, L. D. Brown, W. Zhao, and A. R. Ross, Crustal structure of the Himalayan orogen at 90 east longitude from project INDEPTH deep reflection profiles, *Tectonics*, 17, 481–500, 1998.
- Huang, S., W. Chen, L. Chiao, and T. Tseng, First multi-scale, finite-frequency tomography illuminates 3-D anatomy of the Tibetan Plateau, *Geophys. Res. Lett.*, 37, L06,304–L06,308, 2010.

Jimenez-Munt, I., M. Fernandez, J. Verges, and J. P. Platt, Lithosphere structure underneath the Tibetan Plateau inferred from elevation, gravity and geoid anomalies, *Earth Planet. Sci. Lett.*, 267, 276–289, 2007.

Julia, J., C. J. Ammon, R. B. Hermann, and A. M. Correig, Joint inversion of receiver function and surface wave dispersion observations, *Geophys. J. Int.*, 143, 99–112, 2000.

Kapp, J. L. D., T. M. Harrison, P. Kapp, M. Grove, O. M. Lovera, and D. Lin, Nyainqntanglha shan: A window into the tectonic, thermal, and geochemical evolution of the Lhasa block, southern Tibet, *J. Geophys. Res.*, 110, B08,413, 1–23, 2005.

Kikuchi, M., and H. Kanamori, Inversion of complex body waves, *Bull. Seismol. Soc. Am.*, 72, 491–506, 1982.

Kind, R., et al., Evidence from earthquake data for a partially molten crustal layer in Southern Tibet, *Science*, 274, 1692–1694, 1996.

Kind, R., et al., Seismic images of crust and upper mantle beneath Tibet: Evidence for Eurasian plate subduction, *Science*, 298, 1219–1221, 2002.

Kosarev, L., N. Petersen, L. Vinnik, and S. Roecker, On constraints in the evolution of structures across the Talasso-Fergana fault, *J. Geophys. Res.*, 98, B3:4437–4448, 1993.

Kumar, P., X. Yuan, and R. K. G. Kosarev, The lithosphere-asthenosphere boundary in the Tien Shan-Karakoram region from s receiver functions: Evidence for continental subduction, *Geophys. Res. Lett.*, 32, L07,305, 2005.

Kumar, P., X. Yuan, R. Kind, and J. Ni, Imaging the colliding Indian and Asian lithospheric plates beneath Tibet, *J. Geophys. Res.*, 111, B06,308:1–11, 2006.

Langston, C. A., The effect of planar dipping structure on source and receiver responses for constant ray parameter, *Bull. Seismol. Soc. Am.*, 67, 1029–1050, 1979.

Lei, J., and D. Zhao, Teleseismic p-wave tomography and the upper mantle structure of the central Tien Shan orogenic belt, *Phys. Earth Planet. Inter.*, 162, 165–185, 2007.

Lei, J. S., Seismic tomographic imaging of the crust and upper mantle under the central and western Tien Shan orogenic belt, *J. Geophys. Res.*, 116, B09,305:1–20, 2011.

Li, S., M. J. Unsworth, J. R. Booker, W. Wei, H. Tan, and A. G. Jones, Partial melt or aqueous fluid in the mid-crust of Southern Tibet constrains from INDEPTH magnetotelluric data, *Geophys. J. Int.*, 153, 289–304, 2003.

- Li, X., D. Wei, X. Yuan, R. Kind, P. Kumar, and H. Zhou, Details of the doublet Moho structure beneath Lhasa, Tibet, obtained by comparison of P and S receiver functions, *Bull. Seismol. Soc. Am.*, **101**, 1259–1269, 2011.
- Ligorria, J. P., and C. J. Ammon, Iterative deconvolution and receiver-function estimation, *Bull. Seismol. Soc. Am.*, **85**, 1395–1400, 1999.
- Makovsky, Y., S. L. Klemperer, L. Ratschbacher, L. D. Brown, M. Li, W. Zhao, and F. Meng, INDEPTH wide-angle reflection observation of P-wave-to-S-wave conversion from crustal bright spots in Tibet, *Science*, **274**, 1690–1691, 1996.
- Masek, G. J., B. L. Isacks, E. J. Fielding, and J. Browaeys, Rift flank uplift in Tibet: Evidence for a viscous lower crust, *Tectonics*, **13**, 659–667, 1994.
- McKenzie, D. P., Speculations on the consequences and causes of plate motions, *Royal Astronomical Society Geophysical Journal*, **18**, 1–18, 1969.
- Mejia, J. A., Lithospheric structure beneath the Tibetan Plateau using simultaneous inversion of surface wave dispersion and receiver functions, *Ph.D dissertation at Saint Louis University*, 2001.
- Metivier, F., and Y. Gaudemer, Mass transfer between eastern Tien Shan and adjacent basins(central Asia): Constraints on regional tectonics and topography, *Geophys. J. Int.*, **128**, 1–17, 1997.
- Mitra, S., K. Priestley, A. K. Bhattacharyya, and V. K. Gaur, Crustal structure and earthquake focal depths beneath northeastern India and southern Tibet, *Geophys. J. Int.*, **160**, 227–248, 2005.
- Molnar, P., and S. Ghose, Seismic moments of major earthquakes and the rate of shortening across the Tien Shan, *Geophys. Res. Lett.*, **27**, 2377–2380, 2000.
- Molnar, P., and P. Tapponnier, Active tectonics of Tibet, *J. Geophys. Res.*, **83**, 5361–5375, 1978.
- Molnar, P., P. England, and J. Martinod, Mantle dynamics, uplift of the Tibetan Plateau, and the Indian monsoon, *Review of Geophysics*, **31**, 357–396, 1993.
- Nabelek, J., et al., Underplating in the Himalaya-Tibet collision zone revealed by the HI-CLIMB experiment, *Science*, **325**, 1371–1374, 2009.
- Neil, E. A., and G. A. Houseman, Geodynamics of the Tarim Basin and the Tian Shan in central Asia, *Tectonics*, **16**, 571–584, 1997.
- Nelson, K. D., et al., Partially molten middle crust beneath Southern Tibet: Synthesis of project INDEPTH results, *Science*, **274**, 1684–1687, 1996.
- Nelson, M., R. McCaffrey, and P. Molnar, Source parameters for 11 earthquakes in the Tien Shan, central Asia, determined by P and Sh waveform inversion, *J. Geophys. Res.*, **92**, 12,629–12,649, 1987.

- Ni, J., Contemporary tectonics in the Tien Shan region, *Earth Planet. Sci. Lett.*, **41**, 347–354, 1978.
- Ni, J., and M. Barazangi, Seismotectonics of the Himalayan collision zone: Geometry of the underthrusting Indian Plate beneath the Himalaya, *J. Geophys. Res.*, **89**, 1147–1163, 1984.
- Nowack, R. L., W. Chen, and T. Tseng, Application of gaussian-beam migration to multiscale imaging of the lithosphere beneath the Hi-CLIMB array in Tibet, *bssa*, **100**, 1743–1754, 2010.
- Patriat, P., and J. Achache, India-Eurasia collision chronology has implications for crustal shortening and driving mechanism of plates, *Nature*, **311**, 615–621, 1984.
- Pavlis, X. Y. L., S. Roecker, and F. Vernon, Teleseismic tomographic images of the central Tien Shan, *EOS Trans. AGU*, **84**, 46, 2003.
- Peltzer, G., and P. Tapponnier, Formation and evolution of strike-slip faults, rifts, and basins during the India-Asia collision: An experimental approach, *J. Geophys. Res.*, **93**, 15,085–15,117, 1988.
- Reston, T. J., and M. Perez-Gussinye, Lithophsere extension from rifting to continental breakup at magma-poor margins: rheology, serpentinisation and symmetry, *International Journal of Earth Sciences*, **10**, 1007–1018, 2007.
- Roecker, S. W., T. M. Sabitova, L. P. Vinnik, Y. A. Burmakov, M. I. Golvanov, R. Mamatkanova, and L. Munirova, Three-dimensional elastic wave velocity structure of the western and central Tien Shan, *J. Geophys. Res.*, **98**, 15,779–15,795, 1993.
- Ross, A. R., L. D. Brown, P. Pananont, K. D. Nelson, S. Klemperer, S. Haines, W. Zhao, and J. Guo, Deep reflection surveying in central Tibet: lower-crustal layering and crustal flow, *Geophys. J. Int.*, **156**, 115–128, 2004.
- Royden, L., Coupling and decoupling of crust and mantle in convergent orogens: Implications for strain partitioning in the crust, *J. Geophys. Res.*, **101**, 17,679–17,705, 1996.
- Schulte-Pelkum, V., G. Monsalve, A. Sheehan, M. R. Pandey, S. Sapkota, R. Bilham, and F. Wu, Imaging the indian subcontinent beneath the himalaya, *Nature*, **435**, 1222–1225, 2005.
- Sobel, E., and N. Arnaud, Cretaceous-paleogene basaltic rocks of Te Tuyon Basin, NW China and the Kyrgyz Tien Shan: the trace of a small plume, *Lithos*, **50**, 191–215, 2000.
- Sobel, E., and T. Dumitru, Thrusting and exhumation around the margins of the western Tarim Basin during the India-Asia collision, *J. Geophys. Res.*, **102**, B3:5043–5064, 1997.

- Sol, S., et al., Geodynamics of the southeastern tibetan plateau from seismic anisotropy and geodesy, *Geology*, 35, 563–566, 2007.
- Stratford, W. R., and T. A. Stern, Crust and upper mantle structure of a continental backarc: central north island, new zealand, *Geophys. J. Int.*, 166, 469–484, 2006.
- Tapponnier, P., and P. Molnar, Active faulting and cenozoic tectonics of the Tian Shan, Mongolia, and Baykai regions, *J. Geophys. Res.*, 84, 3425–3459, 1979.
- Tapponnier, P., G. Peltzer, A. Y. L. Dain, R. Armijo, and P. Cobbold, Propagating extrusion tectonics in Asia: New insights from simple experiments with plasticine, *Geology*, 10, 611–616, 1982.
- Thompson, S. C., R. J. Weldon, C. M. Rubin, K. Abdurakhmatov, P. Molnar, and G. W. Berger, Late quaternary slip rates across the central Tien Shan, Kyrgyzstan central Asia, *J. Geophys. Res.*, 107, B9:2203–2212, 2002.
- Tian, X., Q. Wu, Z. Zhang, J. Teng, and R. Zeng, Joint imaging by teleseismic converted and multiple waves and its application in the INDEPTH-III passive seismic array, *Geophys. Res. Lett.*, 32, L21,315–L21,319, 2005.
- Tian, X., D. Zhao, H. Zhang, Y. Tian, and Z. Zhang, Mantle transition zone topography and structure beneath the central Tien Shan orogenic belt, *J. Geophys. Res.*, 115, B10,308: 1–20, 2010.
- Tilmann, F., J. Ni, and I. I. S. Team, Seismic imaging of the downwelling indian lithosphere beneath central tibet, *Science*, 300, 1424–1427, 2003.
- Tseng, T., W. Chen, and R. L. Nowack, Northward thinning of Tibetan crust revealed by virtual seismic profiles, *Geophys. Res. Lett.*, 36, L24,304–L24,309, 2009.
- Vilotte, J. P., M. Daignieres, and R. Madariaga, Numerical modeling of intraplate deformation: Simple mechanical models of continental collision, *J. Geophys. Res.*, 87, 19,709–10,728, 1982.
- Vilotte, J.-P., M. Daignieres, R. Madariaga, and O. Zienkiewicz, The role of a heterogeneous inclusion during continental collision, *Phys. Earth Planet. Inter.*, 36, 236–259, 1984.
- Vinnik, L. P., C. Reigber, I. M. Aleshin, G. L. Kosarev, M. K. Kaban, S. I. Oreshin, and S. W. Roecker, Receiver function tomography of the central tien shan, *Earth Planet. Sci. Lett.*, 225, 131–146, 2004.
- Wittlinger, G., V. Farra, G. Hetenyi, J. Vergne, and J. Nabelek, Seismic velocities in southern Tibet lower crust: a receiver function approach for eclogite detection, *Geophys. J. Int.*, 177, 1037–1049, 2009.

- Wolfe, C., and F. Vernon, Shear-wave splitting at central Tien Shan: evidence for rapid variation of anisotropic patterns, *Geophys. Res. Lett.*, 25, 1217–122–, 1998.
- Wu, Y. C., Evolution of eastern tibet and formation of the plateau, *Paper presented at Converence on Tibetan Plateau, Ministry of Geology and Mineral Resources of PRC*, 1983.
- Xie, J., R. Gok, J. Ni, and Y. Aoki, Lateral variations of crustal seismic attenuation along the INDEPTH profiles in Tibet from Lg Q inversion, *J. Geophys. Res.*, 109, B10,308–B10,325, 2004.
- Xu, J. R., Z. X. Zhao, and Y. Ishikawa, Regional characteristics of crustal stress field and tectonic motions in and around chinese mainland, *Chinese J. Geophys.*, 51, 770–781, 2008.
- Xu, Q., J. Zhao, S. Pei, and H. Liu, The lithosphere-asthenosphere boundary revealed by S-receiver functions from the Hi-CLIMB experiment, *Geophys. J. Int.*, 187, 414–420, 2011.
- Xu, Y., F. Liu, J. Liu, and H. Chen, Crust and upper mantle structure beneath western china from p wave travel time tomography, *J. Geophys. Res.*, 107, B10:2220, 2002.
- Xu, Z. J., and X. D. Song, Joint inversion for crustal and Pn velocities and Moho depth in eastern margin of the Tibetan Plateau, *Tectonophysics*, 491, 185–193, 2010.
- Yang, S., J. Li, and Q. Wang, The deformation pattern and fault rate in the Tianshan Mountains inferred from GPS observations, *Sci. China Ser. D: Earth Sci.*, 51, 1064–1080, 2008.
- Yin, A., Mode of cenozoic east-west extension in Tibet suggesting a common origin of rifts in Asia during the Indo-Asian collision, *J. Geophys. Res.*, 105, 21,745–21,759, 2000.
- Yin, A., and T. M. Harrison, Geologic evolution of the Himalayan-Tibetan orogen, *Science*, 94, 211–280, 2000.
- Yin, A., S. Nie, P. Craig, T. M. Harrison, F. J. R. X. Qian, and G. Yang, Late cenozoic tectonic evolution of the southern chinese tian shan, *Tectonophysics*, 17, 1–27, 1998.
- Zhao, W., and W. J. Morgan, Uplift of Tibetan Plateau, *Tectonics*, 4, 359–369, 1985.
- Zhao, W., K. D. Nelson, J. Che, J. Quo, D. Lu, C. Wu, and X. Liu, Deep seismic reflection evidence for continental underthrusting beneath southern Tibet, *Nature*, 366, 557–559, 1993.

- Zhao, W., et al., Crustal structure of central Tibet as derived from project INDEPTH wide-angle seismic data, *Geophys. J. Int.*, 145, 486–498, 2001.
- Zhu, L., Crustal structure across the Aan Andreas Fault, southern California from teleseismic converted waves, *Earth Planet. Sci. Lett.*, 179, 183–190, 2000.
- Zhu, L., and H. Kanamori, Moho depth variation in southern California from teleseismic receiver functions, *J. Geophys. Res.*, 105, 2969–2980, 2000.

## **Vito Auctoris**

Yuming Zhou was born in Heilong Jiang, China in October, 1984. He attended the Earth and Space Sciences Department of University of Science and Technology of China when he was 20 years old. During his four years of hard study, he went to GPS survey on the Tibetan Plateau and Geology field trip in Anhui Province. He also published a paper in Journal of Geodesy and Geodynamics in 2008. After that, he was first attached to geophysics.

In August 2008, he made his decision to go to the Department of Earth and Atmospheric Sciences of Saint Louis University. During five years of study in Saint Louis University, he processed more than 100000 seismic data recorded in Tibetan Plateau using Perl and Shell scripts and computed P wave receiver function to perform common-conversion-point imaging of crust. He was also involved in an international collaborative fieldwork and deployed 26 broadband seismometers across four provinces in central China. In the last year of his study, he went to Monsanto IT department and worked in the USIT Application Operations Team. He was responsible for monthly releases, Shell scripting and automation systems. Also he managed the Database maintenance, SQL scripting and TM ART monitors. After his internship in Monsanto, he came back to Saint Louis University to finish his Ph.D dissertation and defense.